Northumbria Research Link

CrossMark

Revised Analysis of Fe VII

Alexander Kramida[1,5] ⓘ, Alexander N. Ryabtsev[2] ⓘ, and Peter R. Young[3,4] ⓘ
[1] National Institute of Standards and Technology, Gaithersburg, MD 20899-8422, USA; alexander.kramida@nist.gov
[2] Institute of Spectroscopy, Russian Academy of Sciences, Troitsk, Moscow 108840, Russia
[3] NASA Goddard Space Flight Center, Greenbelt, MD 20771, USA
[4] Northumbria University, Newcastle upon Tyne, NE1 8ST, UK

Abstract

New spectrograms of multiply ionized iron have been recorded and analyzed, targeting the Fe VII spectrum. As a result, several previously unknown spectral lines and energy levels have been identified in this spectrum. These new data have been analyzed together with all previously published laboratory and astrophysical data on this spectrum. The energy levels have been interpreted using parametric calculations with Cowan codes. Radiative transition rates calculated in this work supplemented other previously published calculations in constructing a complete set of recommended transition probabilities. The ionization energy of Fe VII has been redetermined with a fivefold improvement in accuracy. Its new value is $1{,}007{,}928(20)\,\mathrm{cm}^{-1}$, corresponding to $124.9671(25)$ eV.

Supporting material: machine-readable tables

1. Introduction

Six times ionized iron (Fe VII) belongs to the calcium isoelectronic sequence with a $3p^6 3d^2$ ground state electronic configuration. The nine fine-structure levels of the ground configuration give rise to several forbidden transitions in the visible that become prominent in hot, low-density astrophysical plasmas. Examples include planetary nebulae (Perinotto et al. 1999), novae (Darnley et al. 2016), symbiotic stars (Young et al. 2005), active galactic nuclei (Rose et al. 2011), and supernova remnants (Dopita et al. 2016). The fine-structure transitions within the ground ^4F term give lines at 7.8 μm and 9.5 μm that have been observed with the Infrared Space Observatory (Feuchtgruber et al. 1997).

Fe VII has a rich spectrum in the far-ultraviolet as illustrated in Figure 1. This figure shows an Fe VII spectrum generated with version 10 of the CHIANTI database (Del Zanna et al. 2021) assuming a temperature of 0.4 MK, an electron number density of 8×10^8 cm^{-3}, and solar photospheric abundances. The strongest lines are found between 140 and 320 Å and arise from allowed $3p$–$3d$, $3d$–$4p$, $3d$–$4f$, and forbidden $3d$–$4s$ transitions. Between 650 and 1350 Å, there are weaker lines due to $4s$–$4p$, $4p$–$4d$, and $4d$–$4f$ transitions.

The launch of the Extreme ultraviolet (EUV) Imaging Spectrometer (EIS) on board the Hinode spacecraft in 2006 has yielded high-resolution solar spectra in the regions from 170 to 212 Å and from 246 to 292 Å (indicated in Figure 1). Many Fe VII lines were reported by Brown et al. (2008); an atlas of observed spectral lines was published by Landi & Young (2009), and studies have been performed by Young & Landi (2009), Del Zanna (2009), and Young et al. (2021). Discrepancies between observed and predicted line intensities

found in these works have led to questions over the identification of some strong lines. Young et al. (2021) used high-resolution laboratory spectra to confirm identifications in the range between 193 and 197 Å; this range lies at the peak of the EIS sensitivity curve. The present work greatly extends the analysis to cover many of the transitions shown in Figure 1 and to derive new and updated energy levels.

The first Fe VII line identifications date to the 1930s. Bowen & Edlén (1939) classified 42 lines of the $[3p^6]3d^2$–$3d4f$ transition array in the region from 150 to 159 Å. All but $^1S_0$ levels of the ground-level configuration and 17 $3p^6 3d4f$ levels were found. The forbidden transitions calculated from the established $3p^6 3d^2$ energy levels were successively used for the identification of nine lines in the visible spectrum of Nova RR Pictoris. They found that the energy levels of the $3p^6 3d^2$ configuration previously found by Cady (1933) from an identification of the $[3p^6]3d^2$–$3d4p$ transitions are inconsistent with their values, implying that Cady's analysis is incorrect. Except for the $3p^6 3d^2$ levels, the other results of Bowen & Edlén (1939) were not published. Later, Edlén extended the Fe VII analysis, adding the previously missed $3p^6 3d^2\ ^1S_0$ and 10 $3p^6 3d4p$ levels. These levels were included in the compilations by Moore (1952) and by Reader & Sugar (1975). The wavelengths were never published. Fawcett & Cowan (1973) suggested an identification of seven lines in the $3p^6 3d^2$–$3p^5 3d^3$ transition array.

Ekberg (1981) greatly extended the Fe VII analysis. He classified more than 400 lines in the region from 104 to 270 Å and 20 lines in the region from 1010 to 1362 Å. As a result, all levels of the $3p^6 3d4s$ configuration and 141 levels of the $3p^6 3d(4p + nf)$ ($n = 4$–10), $3p^5 3d^2 4s$, and $3p^5 3d^3$ configurations were found.

Faulkner et al. (2001) studied a low-resolution Fe VII spectrum in the range between 680 and 1070 Å excited in ion-rare-gas collisions in an ion beam from an electron cyclotron resonance ion source. They reported an identification of 20 and 7 lines, respectively, in the $[3p^6]3d4p$–$3d4d$ and $3d4d$–$3d4f$ transition arrays. In extension of Ekberg's $3p^6 3d4f$
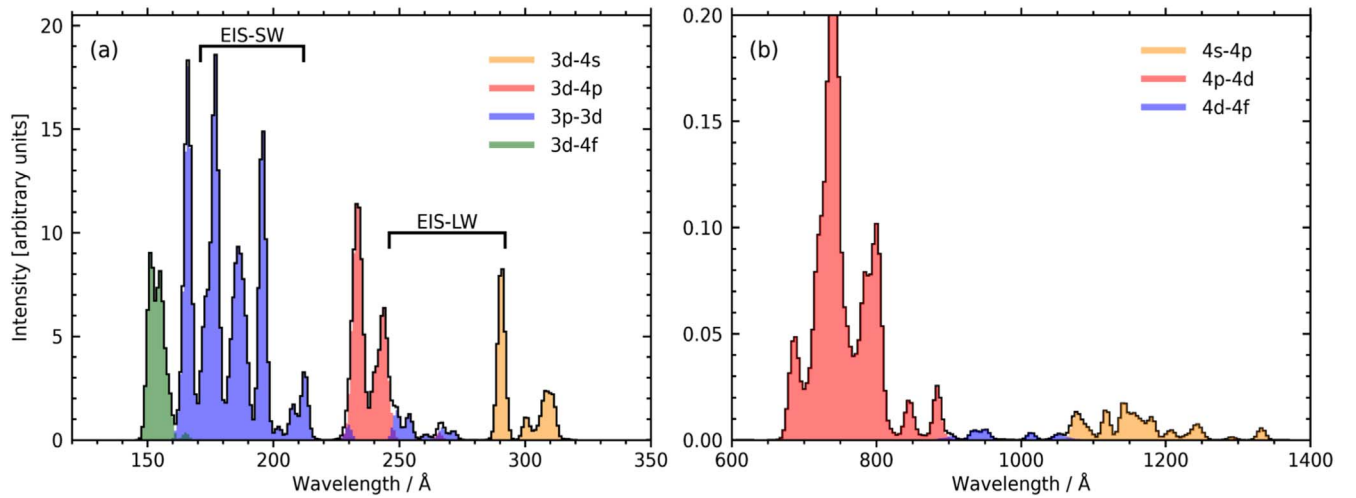
Figure 1. Synthetic Fe VII spectra from CHIANTI for the wavelength ranges (a) 120–350 Å and (b) 600–1400 Å. The black line shows the complete spectrum, and the colored regions show the contributions from the indicated transition arrays. Bin sizes and widths for the lines are set at 1 and 3 Å (a) and at 4 and 12 Å (b). Intensities are in arbitrary units proportional to energy flux per unit wavelength. The spectrum peak in (b) extends outside of the plot with a value of 0.36. Horizontal lines in (a) show the wavelength regions observed by the Extreme-ultraviolet Imaging Spectrometer (EIS) instrument.

levels, the levels of the ^3H term were added. They also listed 15 out of 18 possible $3p^63d4d$ levels. The $[3p^6]3d4p$–$3d4d$ lines were remeasured in high resolution by Ekberg & Feldman (2003) using a vacuum spark source of excitation. The analysis of Faulkner et al. (2001) was revised and extended. As a result, 46 Fe VII lines belonging to the $[3p^6]3d4p$–$3d4d$ transitions were identified, and all levels, except for $^1S_0$, of the $3p^63d4d$ configuration were established.

Liang et al. (2009) observed emission lines in several iron spectra, Fe VI through Fe XIV, in the wavelength range from 125 to 265 Å using the Heidelberg electron beam ion trap (EBIT). Attribution to Fe VII of several previously identified lines was discussed. Spectral resolution was too low and allowed wavelengths to be measured with an accuracy not better than 0.1 Å. At this level of precision, collisional-radiative modeling performed in that work could only roughly reproduce the strongest observed peaks. Transition assignments made by Liang et al. (2009) on the basis of their modeling should be disregarded, as their calculation was too inaccurate to be relied upon.

Beiersdorfer & Träbert (2018) analyzed the iron spectrum in the 165–175 Å range excited in an EBIT at the Lawrence Livermore National Laboratory. They found that six lines around 171 Å identified by Ekberg (1981) might not belong to Fe VII.

Despite large efforts in work on the Fe VII, more laboratory investigations are needed for interpretation of the solar spectrum, as well as of the EBIT spectrum, as was expressed by Young & Landi (2009) and by Liang et al. (2009).

On the theoretical side, the first parametric interpretation of the Fe VII spectrum in terms of Slater's theory was given by Cady (1933). Since then, a few tens of papers have been published on ab initio and semiempirical calculations of the energy structure and radiative rates of this spectrum. A complete listing of these papers can be retrieved from the online bibliographic database of the National Institute of Standards and Technology (NIST; Kramida 2006). The most important of these papers are those of Nussbaumer & Storey (1982) and Li et al. (2018).

Transition probabilities (A values) for allowed and forbidden transitions in Fe VII were critically evaluated by Fuhr et al. (1988). They recommended a set of A values for allowed transitions from Fawcett & Cowan (1973) and Warner & Kirkpatrick (1969a), and for forbidden transitions from Nussbaumer & Storey (1982) and from Warner & Kirkpatrick (1969b). Most of these recommended values were assigned an accuracy category D (uncertainties ⩽50%) and E (uncertainties >50%). The recent calculations of Li et al. (2018) are of much greater accuracy, but they still need to be evaluated. In addition, Kurucz (2010) provided calculated A values for both allowed and forbidden transitions in his online database. One of the aims of the present work is to select the most accurate A values from these data sets and from our own parametric calculations made with Cowan's codes (Cowan 1981; Kramida 2019).

Preliminary results of our Fe VII analysis were announced in a conference paper (Ryabtsev 2017). Application of some of these results to a study of Fe VII emission lines in the spectrum of the Sun in the wavelength range from 193 to 197 Å was presented in a recent article by Young et al. (2021). The present article reports a detailed description and extension of the results of Ryabtsev (2017) together with a critical compilation of available data. Astrophysical implications are discussed.

2. Experimental Data

The experimental data used in the present analysis are comprised from two subsets: (1) laboratory measurements and (2) astrophysical measurements. The spectrograms used are described in Table 1.

In the laboratory, the iron spectrum was excited in a triggered vacuum spark operated with 10 μF or 150 μF capacitors charged with voltages between 1.5 and 9 kV. In a low inductance (80 nH) limit at a peak current of about 50 kA, the vacuum spark plasma emitted the iron ion spectra up to Fe XI. Colder spectra were obtained by the insertion of auxiliary inductance up to 900 nH in the circuit and by changing the voltage. The iron anode was made from a rod of 4 mm diameter, whereas the cathode consisted of a disk of 15 mm diameter with a 1 mm hole drilled in the center followed by a triggering assembly. To provide the spectrum with

Table 1
List of Spectrograms Used in the Present Fe VII Analysis

No.[a]	Date	Instrument[b]	Detector[c]	Range (Å)	Light Source[d]		Data Source[e]
1	1976	ISAN-NIVS	PP Ilford Q2	1015–1300	TVS 4.0 kV	Fe, pure	N/A
	May 7	6.65 m			570 nH		
2	1978	ISAN-GIVS	PP ORWO UV2	124–278	TVS (3.5–9) kV	Fe, pure	N/A
	Jun 20	3 m			(80–570) nH		
3.1	1978	ISAN-GIVS	PP ORWO UV2	179–265	TVS 4.0 kV	Fe + Ti #1	N/A
3.2	Oct 20	3 m		138–214	570 nH	Fe + Ti #2	N/A
4	2014	ISAN-GIVS	IP Fuji BAS-TR	175–355	TVS 4.0 kV	Fe, pure	N/A
	Mar 25	3 m			400 nH		
5	2016	ISAN-GIVS	IP Fuji BAS-TR	118–223	TVS 4.5 kV	Fe, pure	N/A
	Oct 27	3 m			(90–400) nH		
6	2007	Hinode/EIS	CCD	170–211,	Sun		10.5281/zenodo.5224578
	Feb 21			246–291			
7	2000	HST/STIS[f]	CCD+MAMA	1140–7051	RR Tel		https://mast.stsci.edu/
	Oct 18						
8	1999	VLT/UVES	CCD	3085–3914,	RR Tel		10.5281/zenodo.5483961
	Oct 16			4730–6915			

Notes.
[a] Photographic plates recorded at the Institute of Spectroscopy of the Russian Academy of Sciences, Troitsk, Russia (ISAN) contained up to eight tracks, each containing a separate spectrogram exposed with varying conditions of the light source or with the plate holder displaced along the Rowland circle. Two spectrograms recorded on tracks 1 and 2 of the plate No. 3 were exposed at different positions on the Rowland circle and thus covered different overlapping wavelength ranges. They are denoted as 3.1 and 3.2 here. The plate No. 2 also contained two tracks, but their covered wavelength regions had a very small overlap. Thus, both of these tracks are united here under the same No. 2.
[b] Acronyms used in the description of instruments: ISAN—see note (a) above; NIVS/GIFS—normal/grazing incidence spectrograph with a 6.65 m/3 m grating, respectively; EIS—EUV Imaging Spectrometer on board Hinode satellite (see http://solarb.mssl.ucl.ac.uk/eiswiki/); HST—Hubble Space Telescope; STIS—Space Telescope Imaging Spectrograph; VLT—Very Large Telescope (Kueyen), Paranal Observatory, Chile.
[c] Acronyms used in the description of the detectors: PP—Photographic Plate; IP—phosphor Imaging Plate; CCD—Charge-Coupled Device; MAMA—Multi-Anode Microchannel detector Array.
[d] Acronyms used in the description of the light sources: TVS—triggered vacuum spark (discharge of a 10 μF capacitor with the specified voltage and inductance inserted in series in the circuit; the material of the electrodes is specified for each spectrogram); RR Tel—the nebula RR Telescopii.
[e] The spectrograms #1–5 are archived at ISAN (Troitsk, Russia).
[f] The HST/STIS data used here consist of 16 data files that can be identified in the Barbara A. Mikulski Archive for Space Telescopes (MAST) by the proposal ID 8098.

reference lines, the iron cathode was replaced by a titanium one in some exposures.

For the region between 90 and 350 Å, a grazing incidence 3 m spectrograph was used. A grating ruled with 3600 lines mm^{-1} installed at a grazing angle of 5° provides plate factors varying in the range from 0.25 to 0.46 Å mm^{-1} over the region of observation. Previous spectrograms taken for the analysis of Fe VIII (Ramonas & Ryabtsev 1980) were recorded on ORWO[6] UV-2 photographic plates. These plates were scanned on an EPSON EXPRESSION scanner and then digitized and measured using the Gfit code (Engström 1998). It was known from our measurement of a calibrated length scale that our scanner possessed almost sinusoidal periodic errors with an amplitude of 0.02 mm and a period of 50 mm. In the early measurements, a correction of these periodic scanner errors was performed by a simultaneous scanning of a photographic plate and a calibrated length scale. After a valuable study of the use of a commercial flatbed scanner for digitizing photographic plates by Wyatt & Nave (2017), the plates were placed along the short side of the scanner to eliminate large periodic scanning errors.

A set of new spectra (spectrograms Nos. 4 and 5 in Table 1) was obtained using phosphor imaging plates (Fuji BAS-TR; Ryabtsev 2017). These spectra were scanned with a Typhoon

FLA 9500 reader using a 10 μm sample step. The images produced were processed and analyzed with the ImageQuant TL 7.0 image analysis software. The spectrum was further reduced using the GFit code (Engström 1998). A spectrum stored on an imaging plate can be retrieved several times with reduced intensity each time. However, the reduction of the spectrum intensity in the second scan was not drastic, and due to the large dynamic intensity range of the imaging plates, most of the lines could be measured in the second scan. This property of an imaging plate was used to check for possible scanning errors of our FLA 9500 reader. The same spectrogram was scanned the first time with the imaging plate oriented along the longer side of the flatbed of the reader and the second time along the shorter side. No regular scanning errors were seen in a comparison of the relative line positions along the spectrum.

The FWHM intensities of the iron lines change from Fe VII to Fe XI. They are the largest for Fe XI and slightly change with the spark peak current. On average along the spectrum, the Fe VII line widths are 0.015 Å and 0.025 Å, respectively, on photographic plates and imaging plates. Although they have worse resolution, the imaging plate spectrograms possess a high linearity of the line intensities. Therefore, the wavelengths were measured using the photographic plates, whereas the line intensity data were obtained from the imaging plate spectrograms. The linearity of the imaging plates was useful in the distinction of the lines belonging to different iron ions by the

---

[6] The identification of commercial products in this paper does not imply recommendation or endorsement by the National Institute of Standards and Technology, nor does it imply that the items identified are necessarily the best available for the purpose.

observation of the changes of the line intensities with variation of the discharge conditions.

The iron wavelengths were measured using titanium ion lines (Svensson & Ekberg 1969) as standards on the photographic plate spectrograms, taken with an iron anode and a titanium cathode of the spark. The rms deviation of the reference titanium lines from the calibration curve was 0.002 Å, while Svensson & Ekberg (1969) claimed an uncertainty of ±0.004 Å for their wavelengths. By comparing the observed wavelengths listed by Svensson & Ekberg (1969) with the Ritz wavelengths of the NIST Atomic Spectra Database (ASD; Kramida et al. 2020), we established that the measurements of Svensson & Ekberg (1969) in the region between 151 and 268 Å are accurate to ±0.0017 Å on average, while their uncertainty for longer wavelengths increases to their specified value of ±0.004 Å. The total uncertainty of wavelengths for unperturbed (i.e., symmetrical, isolated, and not blended) lines measured on Fe + Ti spectrograms was found to be about ±0.0027 and ±0.0029 Å on the two best photographic plates used in our final wavelength reduction. One spectrogram, taken with both electrodes made of iron, was reduced using internal standards transferred from the Fe + Ti spectrograms. For this spectrogram, the total wavelength uncertainty of unperturbed lines was found to be only slightly larger, about ±0.003 Å. Uncertainties for perturbed lines were estimated by comparisons with Ritz wavelengths calculated in the present analysis. They vary from ±0.004 to ±0.010 Å.

One photographic plate (No. 1 in Table 1) containing a vacuum spark spectrum in the region from 1015 to 1300 Å recorded on a 6.65 m normal incidence spectrograph was also measured. With a 1200 lines mm^{-1} grating, the spectrograph has a plate factor of 1.25 Å mm^{-1}. The lines of Fe V (Kramida 2014a), Fe VI (Ekberg 1975), and spark impurities C III and Si III (Kramida et al. 2020) were used as standards in this region. The rms deviation 0.006 Å of the standard lines from a polynomial calibration curve was accepted as the statistical uncertainty of the measurements. In the geometry of the normal incidence setup, astigmatism was low, which led to a significant polar effect. This means that emission of different species was separated in the space between the anode and the cathode, and this separation was projected onto the photographic plate. On the one hand, it helped us to identify the different ionization stages responsible for the lines, but on the other hand, this could cause systematic shifts on the measured wavelengths. Indeed, such shifts were revealed by comparison of our measured wavelengths with those of Ekberg & Feldman (2003), as shown in Figure 2.

The weighted mean of the differences shown in Figure 2 is 0.007(2) Å. We interpreted it as a systematic shift in our measurements (caused by the polar effect mentioned above) and have removed it from the original wavelength values.

The final wavelength values for Fe VII lines adopted in our analysis were taken as a weighted average of our measurements and those of other authors (Ekberg 1981; Ekberg & Feldman 2003; Landi & Young 2009) where the latter are available. In all cases where weighted averaging was made for the wavelengths, the weights used were the inverse squares of the measurement uncertainties. Determination of the uncertainty of the weighted mean is a nontrivial problem for spectroscopic measurements, which often contain undetected systematic errors due to line blending, photographic plate deformations, and other effects that elude detection. As a result, in sets of measured wavelengths, it is usual to see a few that have
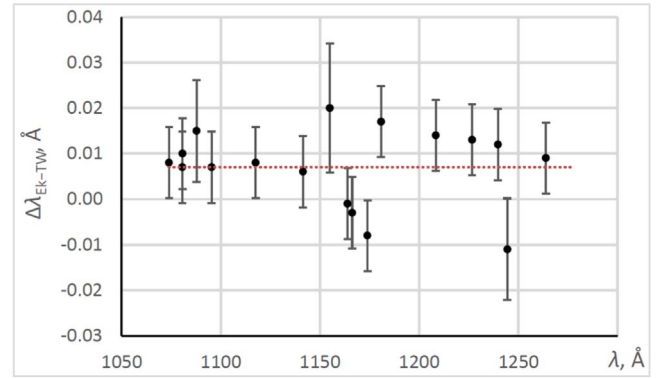
Figure 2. Differences between Fe VII wavelengths measured by Ekberg & Feldman (2003) and our original values from the normal incidence spectrogram. The error bars are a combination in quadrature of our statistical uncertainty, ±0.006 Å for unperturbed lines, with the total uncertainty of Ekberg & Feldman (2003), ±0.005 Å. Uncertainties have been increased for a few lines found to be blended. The dotted line shows the systematic shift attributed to our measurement.

inexplicably large deviations from other independent measurements of similar accuracy. Averaging reduces the errors present in such discrepant measurements, but the uncertainty of the mean wavelength must reflect the presence of discrepancies in the individual values. Since such discrepancies are caused by unknown quasi-random systematic effects, there is no rigorous statistical treatment for them. Nevertheless, many practical recipes exist in the literature. We find the one developed by Radziemski & Kaufman (1969) to be the most useful and reasonable. Their formula for the uncertainty of the weighted mean u_{wm}, adapted by Kramida (2011), reads as follows:

$$u_{\text{wm}} = \frac{\left[\sum(w_i + w_i^2 r_i^2)\right]^{1/2}}{\sum w_i}, \qquad (1)$$

where w_i is the weight of the ith measurement ($w_i = u_i^{-2}$, u_i being the uncertainty of that measurement), and r_i is the difference of the ith measurement from the weighted mean. We applied this Equation (1) to determine the uncertainties of all weighted mean values used in the present work.

It should be noted that in the grazing incidence region, instead of wavelengths listed by Ekberg (1981), we used wavelengths restored from his listed wavenumbers, since they were given with greater precision. The estimated uncertainty of the final wavelengths in the grazing incidence region is between ±0.0013 and ±0.011 Å, except for one line at 271.03(4) Å observed only in the solar spectrum (Landi & Young 2009), where it is severely blended by O V. In the normal incidence region, the uncertainties vary between ±0.004 and ±0.015 Å, except for a few lines observed only by Faulkner et al. (2001). The latter were estimated to be between ±1 and ±2 Å, which is based on comparison with more precise values from other authors. A few of the identifications given by Faulkner et al. (2001) have been corrected here, as indicated by Ekberg & Feldman (2003) and by the present analysis.

The wavelengths affected by the present measurements and by averaging made in the present work are collected in Tables 2 and 3. The mean values given in the last columns of these tables have been supplemented by wavelengths compiled from other laboratory and astrophysical sources. The complete list of all identified lines is given in Table 3.

Table 2
Observed Lines of Fe VII in the Region from 158 to 290 Å

λ_{TW}[a] Fe Pure (Å)	λ_{TW}[a] Fe + Ti #1 (Å)	λ_{TW}[a] Fe + Ti #2 (Å)	I_{TW}[b] (arb. units)	λ_{E81}[c] (Å)	I_{E81}[d]	λ_{LY09}[e] (Å)	I_{LY09}[e]	λ_{mean}[f] (Å)
158.6556(38)		158.6575(34)	4					158.6567(42)
160.5070(38)			3					160.5070(50)
163.1829(30)		163.1810(29)	101	163.1830(22)	7			163.1824(16)
182.0681(30)	182.0694(27)	182.0693(29)	106	182.0711(22)	5	182.0745(94)	23	182.0698(14)
				182.2211(22)	2			182.2211(22)
182.4058(30)	182.4065(27)	182.4067(29)	77			182.4054(74)	22	182.4063(16)
182.7388(30)	182.7388(27)	182.7378(29)	77	182.7399(22)	4	182.7304(75)	11	182.7387(14)
182.8277(38)	182.8281(62)	182.8277(34)	37					182.8278(40)
183.5330(30)	183.5374(27)	183.5381(29)	70	183.5391(22)	6	183.5413(57)	12	183.5375(16)
183.8185(30)	183.8242(27)	183.8229(29)	260	183.8249(22)	9	183.8242(34)	91	183.8232(16)
248.4240(30)	248.4290(27)		7					248.4268(27)
						248.6345(48)	35	248.6345(48)
248.7410(30)			3	248.7430(22)	2			248.7423(19)
						249.2954(48)	70	249.2954(48)
						253.5208(48)	19	253.5208(48)
						254.0508(82)	49	254.0508(82)
254.3447(30)			12					254.3447(30)
						260.6719(49)	20	260.6719(49)
265.6966(30)			120	265.6969(22)	8			265.6968(18)
						267.209(10)	14	267.209(10)
						267.2670(90)	20	267.2670(90)
				270.3629(22)	0			270.3629(22)
						271.031(41)	18	271.031(41)
						271.6924(45)	25	271.6924(45)
						289.6880(59)	38	289.6880(59)
						289.8449(53)	37	289.8449(53)
						290.3059(53)	70	290.3059(53)
						290.7518(89)	179	290.7518(89)

Notes.

[a] Wavelengths measured in this work (TW) on three spectrograms: Fe pure—photographic plate exposed with spark electrodes made of pure iron; Fe + Ti #1 and Fe + Ti #2—photographic plates exposed with spark electrodes made of Fe (anode) and Ti (cathode) with different voltages and currents. Total measurement uncertainties are given in parentheses in units of the last decimal place of the value.

[b] Intensities observed in this work recorded on an imaging plate with both spark electrodes made of Fe.

[c] Wavelengths measured by Ekberg (1981) have been restored from the wavenumbers given therein in the same table as wavelengths but with a greater precision. The total measurement uncertainties, given in parentheses in units of the last decimal place of the value, have been evaluated in the present work.

[d] Observed intensities as reported by Ekberg (1981), in arbitrary units on a logarithmic scale.

[e] Wavelengths and intensities measured by Landi & Young (2009) in the solar spectrum (see the text). The solar intensities are in units of $\mathrm{erg\,cm^{-2}\,s^{-1}\,sr^{-1}}$ ($=0.001\ \mathrm{J\,m^{-2}\,s^{-1}\,sr^{-1}}$).

[f] The weights used in the averaging were reciprocal squared uncertainties of the measurements. Uncertainties of the mean values were determined with the formula of Radziemski & Kaufman (1969; see the text and Equation (1)).

(This table is available in its entirety in machine-readable form.)

Reference wavelengths for the forbidden lines within the ground configuration come from astrophysical sources. The $^3F_3$–$^3F_4$ and $^3F_2$–$^3F_3$ ground-term splittings occur in the infrared at 7.8 μm and 9.5 μm, respectively, and were measured by Feuchtgruber et al. (1997). Young et al. (2005) listed 13 Fe VII lines in ultraviolet and visible spectra of the symbiotic star RR Telescopii. Updated wavelengths for these lines were derived for the present work by fitting Gaussian functions to the lines and using the wavelength calibration method described in (Young et al. 2011). The lines at 2143, 5159, 5276, and 6087 Å were partly blended with other species, and two-Gaussian fits were performed to resolve the blends. The three shortest-wavelength lines (decays from the $^1S_0$ level) were observed with the Space Telescope Imaging Spectrograph (STIS) on the Hubble Space Telescope (HST). Nine of the remaining lines were observed at visible wavelengths with the Ultraviolet Echelle Spectrograph (UVES) of the Very Large Telescope. The line at 4699 Å lies within a coverage gap of UVES,

but was observed at low resolution with HST. Its rest wavelength was determined by multiplying the observed value given in Table 2 of Young et al. (2005) by a correction factor calculated as the mean of the ratios of the newly derived UVES values to the original observed wavelengths of Young et al. (2005). The two lines at 5721 and 6087 Å were given with an accuracy comparable to UVES measurements by Bowen (1960). For this work, they have been averaged with the UVES measurements that yielded values of (5721.20 ± 0.11) and (6086.92 ± 0.12) Å (air).

We also note that the rest wavelength of the Fe VII line at 196.2126(29) Å was incorrectly stated to be 196.217 Å in (Young & Landi 2009). The presently used wavelength of this line was obtained from the observed value 196.239 Å (Landi & Young 2009) by applying the Doppler shift correction corresponding to the velocity of $-40.4(45)\ \mathrm{km\,s^{-1}}$. This velocity was determined by Young & Landi (2009) from a large set of observed lines of different species. In deriving the wavelength of

Table 3
Observed Lines of Fe VII in the Region from 1073 to 1278 Å

$\lambda_{\text{TW,orig}}$ [a] (Å)	I_{TW} [b] (arb. units)	Char. [c]	λ_{E81} [d] (Å)	$\Delta\lambda_{\text{E81}-\text{TW}}$ [e] (Å)	$\lambda_{\text{TW,corr}}$ [f] (Å)	λ_{mean} [g] (Å)
1073.945(6)	187		1073.953(5)	0.008(8)	1073.952(6)	1073.953(4)
1080.630(6)	55		1080.637(5)	0.007(8)	1080.637(6)	1080.637(4)
1080.726(6)	44		1080.736(5)	0.010(8)	1080.733(6)	1080.735(4)
1081.216(10)	47	q			1081.223(10)	1081.223(10)
1087.846(10)	172	bl	1087.861(5)	0.015(11)	1087.853(10)	1087.859(5)
1095.336(6)	283		1095.343(5)	0.007(8)	1095.343(6)	1095.343(4)
1117.572(6)	437		1117.580(5)	0.008(8)	1117.579(6)	1117.580(4)
1141.429(6)	531		1141.435(5)	0.006(8)	1141.436(6)	1141.435(4)
1145.030(6)	310				1145.037(6)	1145.037(6)
1146.892(6)	47				1146.899(6)	1146.899(6)
1154.972(10)	147	bl	1154.992(10)	0.020(14)	1154.979(10)	1154.986(8)
1163.880(6)	94		1163.879(5)	−0.001(8)	1163.887(6)	1163.882(5)
1166.186(6)	276		1166.183(5)	−0.003(8)	1166.193(6)	1166.187(5)
1166.294(6)	106				1166.301(6)	1166.301(6)
1171.651(6)	45				1171.658(6)	1171.658(6)
1173.770(6)	69				1173.777(6)	1173.777(6)
1173.923(6)	53		1173.915(5)	-0.008(8)	1173.930(6)	1173.921(6)
1174.044(6)	118				1174.051(6)	1174.051(6)
1180.806(6)	133		1180.823(5)	0.017(8)	1180.813(6)	1180.819(5)
1208.361(6)	99		1208.375(5)	0.014(8)	1208.368(6)	1208.372(5)
1226.640(6)	204		1226.653(5)	0.013(8)	1226.647(6)	1226.651(4)
1239.678(6)	195		1239.690(5)	0.012(8)	1239.685(6)	1239.688(4)
1244.453(10)	71	S	1244.442(5)	-0.011(11)	1244.460(10)	1244.445(6)
1256.246(10)	155	w			1256.253(10)	1256.253(10)
1263.835(6)	18		1263.844(5)	0.009(8)	1263.842(6)	1263.843(4)
1265.004(6)	172				1265.011(6)	1265.011(6)
1265.982(6)	333				1265.989(6)	1265.989(6)
1270.134(6)	126				1270.141(6)	1270.141(6)
1277.781(6)	96				1277.788(6)	1277.788(6)

Notes. The numbers in parentheses are standard uncertainties in units of the last decimal place of the value.
[a] Wavelengths measured on a photographic plate recorded in this work with a normal incidence spectrograph.
[b] Intensities of lines recorded on a photographic plate were measured photoelectrically. They are not corrected for nonlinearity of response of the photographic plate to exposure, nor for spectral dependence of sensitivity of the emulsion.
[c] Line character: bl—blended; S—a weak feature on a shoulder of a stronger line; w—wide line; q—asymmetric line.
[d] Wavelength reported by Ekberg (1981) with our estimate of its uncertainty.
[e] Differences between measurements of Ekberg (1981) and our original values from the first column. Their weighted mean is 0.007(2) Å.
[f] Our measured wavelength increased by 0.007 Å to make it consistent with Ekberg (1981).
[g] The weights used in the averaging were reciprocal squared uncertainties of the measurements. Uncertainties of the mean values were determined with the formula of Radziemski & Kaufman (1969; see the text and Equation (1)).

the 196.217 Å line, those authors mistakenly used a different velocity correction. This error also affected the energy level values given in Table 3 of Young & Landi (2009).

3. Main Results

The Fe VII spectrum analysis was guided by calculations of the energy levels and transition probabilities with a suite of Cowan codes (Cowan 1981; Kramida 2019). For the initial analysis, we used the following sets of interacting configurations: $[\text{Ne}]3s^23p^6(3d^2 + 3d4s + 3d4d + 4s^2) + 3s3p^63d^3 + 3s^23p^43d^4$ of even parity and $[\text{Ne}]3s^23p^6[3dnp(n=4,5) + 3dnf(n=4\text{–}7) + 4s4p + 4s4f + 4d4p + 4d4f] + 3s^23p^5(3d^3 + 3d^24s + 3d4s^2 + 3d^24d) + 3s3p^53d^4 + 3s^23p^33d^5$ of odd parity. The calculated energy levels were fitted to the experimental levels from Ekberg (1981) and Ekberg & Feldman (2003). Thus obtained energy levels and transition probabilities were used as entries to a program for visual identification of spectral lines and energy levels in optical spectra (IDEN2; Azarov et al. 2018).

The main emphasis was put on verification and extension of the previous analyses of the resonance $([\text{Ne}]3s^2)3p^63d^2$–$(3p^53d^3 + 3d4p)$ transitions in the range from 150 to 300 Å. In the following, we will discuss the results of our identification summarized in Table 4 (wavelengths) and Table 5 (energy levels). Since no energy levels involving excitation from the $3s$ and lower electronic shells have been observed in experiments, the designations of the complete $[\text{Ne}]3s^2$ core shells are omitted from level labels in the subsequent text and Table 5.

All but one energy level found by Ekberg (1981) were confirmed. A level designated as $(a^2D)^1D_2^\circ$ at 538,290 cm^{-1} was discarded. It was based in Ekberg (1981) on three lines: 185.773, 192.006, and 193.421 Å. The strongest line at 192.006 Å, representing the $3p^63d^2$ $^1D_2$-$3p^53d^3(^2D2)$ $^1D_2^\circ$ transition, was previously (Ramonas & Ryabtsev 1980) identified as Fe VIII, and it shows a character of this ion on our spectrograms. The other two lines, being very weak, could belong to the ions of a lower ionization stage than Fe VII. Our calculations predict the $^1D_2$–$(^2D2)^1D_2^\circ$ transition at about 191.8 Å. There is an unidentified line

Table 4
Spectral Lines of Fe VII

$\lambda_{\rm obs}$[a] (Å)	$I_{\rm obs}$[b] (arb. units)	Char.[c]	$\lambda_{\rm Ritz}$[a] (Å)	$\Delta\lambda_{\rm o-c}$[d] (Å)	J_1[e]	J_2[e]	N_1[e]	N_2[e]	E_1[e] (cm^{-1})	E_2[e] (cm^{-1})	T[f]	gA[g] (s^{-1})	Ac[h]	TP Ref.[i]	Line Ref.[i]	Wt[j]	Com[k]
104.838(3)	3		104.838(3)		3	4	2	207	1049.75	954,900		6.01E+10	D+	K10	E81		S
207.8311(18)	200	*	207.8335(11)	−0.0024	4	3	8	59	28,923.5	510,078		9.24E+07	E	TW	E81,TW	0.428	
207.8311(18)	200	*	207.8349(12)	−0.0038	0	1	9	67	67,076.9	548,228		3.08E+08	C+	TW	E81,TW	0.572	
681.416(7)	120		681.418(6)	−0.002	1	0	26	91	425,127.1	571,879.9		1.60E+09	D+	K10	EF03		
6086.92(8)	871	bl(Ca V)	6086.87(6)	0.05	3	2	2	4	1049.75	17,474.00	M1	2.88E+00	C	N82	TW,B60		
			257,200(300)		0	1	5	6	20,040.0	20,428.8	M1	3.16E-03	AA	N82			P

Notes. The numbers in parentheses are standard uncertainties in units of the last decimal place of the value.

[a] Observed and Ritz wavelengths between 2000 and 20000 Å are given in standard air; outside this range, they are in vacuum. Conversion between vacuum and air wavelength was made with the five-parameter formula from Peck & Reeder (1972).

[b] Observed intensities are given on a linear scale proportional to total energy flux under the line contour (see the text), except for the forbidden lines above 1400 Å, for which the intensities are quoted from Young et al. (2005), rounded to integers.

[c] Character of the observed line in the source where the wavelength was measured: *—intensity is shared by two or more transitions; bl—blended line (the blending species are given in parentheses where known); i—identification is uncertain; m—masked by a stronger line; p—perturbed by a nearby line (both the wavelength and intensity may be affected); q—asymmetric line; w—wide line.

[d] Difference between the observed and Ritz wavelengths (blank for unobserved lines and for lines that solely determine one of the levels involved).

[e] Total angular momentum quantum numbers, sequential indexes (defined in the last column of Table 5), and excitation energies of the lower and upper levels.

[f] Transition type: blank—electric dipole; M1—magnetic dipole; E2—electric quadrupole; M1+E2—mixed type (both M1 and E2 transitions contribute to intensity).

[g] Weighted transition probability ($g = 2J_2 + 1$ is the statistical weight of the upper level).

[h] Transition probability accuracy as defined by NIST (see https://physics.nist.gov/PhysRefData/ASD/Html/lineshelp.html#OUTACC).

[i] Transition probability and observed wavelength source references: B60—Bowen (1960); B08—Brown et al. (2008); D09—Del Zanna (2009); E81—Ekberg (1981); EF03—Ekberg & Feldman (2003); F97—Feuchtgruber et al. (1997); F01—Faulkner et al. (2001); K10—Kurucz (2010); L09—Landi & Young (2009); L18—Li et al. (2018); M97—McKenna et al. (1997); N82—Nussbaumer & Storey (1982); TW—this work; Y05—Young et al. (2005); Y09—Young & Landi (2009); Y21—Young et al. (2021).

[j] Weight of transition in the level optimization procedure (defined only for multiply classified lines).

[k] Comments: M—masked; P—predicted; S—observed transition that solely defines one of the levels involved; X—excluded from the level optimization procedure, in addition to masked and predicted lines, which are also excluded.

(This table is available in its entirety in machine-readable form.)

Table 5
Energy Levels of Fe VII

Conf.[a]	Term[a]	J	Level (cm⁻¹)[b]	Perc.[a]	Perc. 2[a]	Conf. 2[a]	Term 2[a]	Perc. 3[a]	Conf. 3[a]	Term 3[a]	Ref.[c]	O − C[d]	N_{lin}[e]	Index
$3p^63d^2$	^3F	2	0	98							SC85,E81	−7	67	1
$3p^63d^2$	^3F	3	1049.75(11)	98							E81	7	87	2
$3p^63d^2$	^3F	4	2329.48(20)	98							E81	−1	71	3
$3p^63d^2$	^1D	2	17,474.00(18)	91	6	$3p^63d^2$	^3P				E81	1	72	4
$3p^63d^2$	^3P	0	20,040.0(4)	98							E81	5	20	5
$3p^53d^3(^4P)$	$^5S°$	2	389,340(6)	99							LY09	−172	2	14
$3p^53d^3(^4F)$	$^5D°$	2	395,434(13)	58	33	$3p^53d^3(^4P)$	$^5D°$	8	$3p^53d^3(^4F)$	$^5F°$	YL09	82	1	15
$3p^53d^3(^4F)$	$^5D°$	3	395497(8)	52	35	$3p^53d^3(^4P)$	$^5D°$	12	$3p^53d^3(^4F)$	$^5F°$	LY09	29	2	16
$3p^53d^3(^4F)$	$^5D°$	1	395,515(19)	64	32	$3p^53d^3(^4P)$	$^5D°$				YL09	93	1	17
$3p^53d^3(^4F)$	$^5D°$	4	395,952(13)	47	40	$3p^53d^3(^4P)$	$^5D°$	12	$3p^53d^3(^4F)$	$^5F°$	LY09	−35	1	18
$3p^53d^3(^4F)$	$^5F°$	5	403,460(8)	94	5	$3p^53d^3(^4P)$	$^5G°$				YL09	4	1	19
$3p^53d^3(^4F)$	$^5F°$	4	404,526(8)	81	7	$3p^53d^3(^4P)$	$^5D°$	5	$3p^53d^3(^4F)$	$^5G°$	YL09	147	1	20
$3p^53d^3(^4F)$	$^5F°$	3	404,900(7)	82	7	$3p^53d^3(^4P)$	$^5D°$	5	$3p^53d^3(^4F)$	$^5D°$	YL09	252	1	21
$3p^53d^3(^2G)$	$^3F°$	3	423,286.9(6)	42	16	$3p^53d^3(^4F)$	$^3F°$	13	$3p^53d^3(^4F)$	$^5G°$	TW	83	3	22
$3p^53d^3(^4F)$	$^5G°$	2	424,077.4(6)	54	21	$3p^53d^3(^2G)$	$^3F°$	9	$3p^63d4p$	$^3F°$	TW	151	3	23

Notes.

[a] Configuration, LS term labels, and percentages of the three leading components in the eigenvector of each level. The intermediate term $^2P°$ of the $3p^5$ subshell is omitted from the configuration labels for brevity. For several levels, the configuration and term labels given in the first two columns correspond to the second, third, fourth, or fifth leading component. This reordering of the eigenvector components was necessary to make the configuration and term labels unique for each J value. Additional quantum numbers 1 and 2 after the ^2D term labels of the $3d^3$ subshell are the indexes of Nielson & Koster (1963).

[b] Standard uncertainties are given in parentheses in units of the last decimal place of the value. For example, 551,567.0(34) means $551,567.0 \pm 3.4$. A question mark after the value 539,427(5) means that identification of this level is questionable (see the text). An additional digit is retained in some level values when it was necessary to reproduce precisely measured wavelengths.

[c] Key to references for the first identification of the level: E81—Ekberg (1981); EF03—Ekberg & Feldman (2003); F01—Faulkner et al. (2001); LY09—Landi & Young (2009); SC85—Sugar & Corliss (1985); YL09—Young & Landi (2009); TW—this work; all level values and their uncertainties have been determined in the present work (see the text).

[d] Residual ("obs. − calc.") of the parametric least-squares fit with Cowan's codes (in units of cm^{-1}).

[e] Number of observed lines determining the level value in the least-squares optimization procedure.

(This table is available in its entirety in machine-readable form.)

with the Fe VII properties at 191.590 Å that could be this transition, giving the level energy 539,427 cm^{-1}. The line can be blended by the Fe VI line at 191.580 Å (Azarov et al. 1996). However, the Fe VI line is relatively weak, and its influence on the wavelength and intensity of the proposed Fe VII line is expected to be small. The line is listed in Table 4 with a character "i" (uncertain identification), and the level was not used in the fitting.

For one other line observed by Ekberg (1981) at 233.015 Å, we changed the identification, since our calculations yield a negligibly small intensity contribution from the transition assigned by Ekberg to this line.

The remaining 162 lines of Ekberg in our observed spectral range (145 in the region between 158.6 and 291 Å and 17 between 1070 and 1300 Å) were accepted, including several very weak ones not observed on our plates (see Tables 2 and 3). They are not seen in our spectra possibly because of a higher background level, but they fit well to the transition arrays from the corresponding levels. Assignments of several lines given in Table 4 with the line reference "E81,TW" were changed in accordance with a change of the designation for the involved levels, which will be discussed below. We identified 65 new lines of the resonance transition array. These lines have a line reference "TW" in Table 4. Most of the new lines belong to a low part of the $3p^5 3d^3$ configuration where it overlaps and strongly interacts with the $3p^6 3d4p$ configuration.

Table 4 also contains a compilation of all known Fe VII lines up to 95267 Å with a reference for each line, as well as several predicted lines that have not been observed. It should be noted that the wavelengths in the RR Telescopii spectrum published by Young et al. (2005) were refined by one of us (P.R.Y.) prior to being included in Table 4.

As mentioned above, the iron spark spectrum was also measured in the region of the $(3p^6)3d4s$–$3d4p$ transitions in an effort to find the transitions from newly identified $3p^5 3d^3$ levels having the wave functions mixed with the $3p^6 3d4p$ configuration. All 17 lines identified by Ekberg & Feldman (2003) in the range between 1070 and 1300 Å are present in our spectrum (see Table 3). Three lines at 1010.260, 1016.072, and 1332.381 Å listed by Ekberg & Feldman (2003) are outside of our observation range. The analysis of Ekberg & Feldman (2003) was extended by the addition of 12 new lines. They support the identification of all 10 new levels with energies in the range from 423,000 cm^{-1} to 433,000 cm^{-1}. Two additional lines (not included in Table 3) can be attributed to transitions from the level at 427,870 cm^{-1} to $3p^6 3d4s$ levels, but their character on our recordings does not allow us to attribute them to Fe VII with confidence. Therefore, we consider this level as questionable.

Faulkner et al. (2001) observed some emission lines of Fe VII excited in the collision of an Fe^{7+} ion beam with helium and argon targets. They classified a partially resolved structure near 1000 Å as the $(3p^6)3d4d$ $^3G3d4f$ ^3H multiplet. In accordance with our calculations and using the $3p^6 3d4d$ ^3G level classifications by Ekberg & Feldman (2003), we revised the identification of the 1001.7 and 999.6 Å peaks given by Faulkner et al. (2001). The former one is now attributed to the $^3G_5$-$^3H_6$ transition, whereas the latter one is interpreted as a blend of the $^3G_4$-$^3H_5$ and $^3G_3$-$^3H_4$ transitions. By comparing the wavelengths listed by Faulkner et al. (2001) with the much more accurate measurements of Ekberg & Feldman (2003), we found that the uncertainty of wavelengths measured by Faulkner et al. (2001) is about 1.0 Å for isolated lines, but increases up to 2 Å for partially resolved lines.

In total, eight lines observed by Faulkner et al. (2001) but not by any other authors have been included in Table 4 with revised identifications for six of them.

The energy level values in Table 5 were obtained by using the program LOPT for least-squares optimization of energy levels (Kramida 2011) with the wavelengths of Table 4. The Ritz wavelengths of transitions and their uncertainties are also determined by that program. Table 5 also shows the number of lines included in the optimization of each level.

As noted in Section 1, Landi & Young (2009) created an atlas of solar spectral lines recorded by EIS on board the Hinode satellite. Those authors succeeded in making several new Fe VII line identifications (Young & Landi 2009). It should be mentioned that the present analysis permitted four new Fe VII lines in the EIS spectrum to be added to their identifications. The rest wavelengths of these lines reported by Landi & Young (2009) are 182.405, 209.425, 209.732, and 245.937 Å. The line at 209.425 Å is possibly affected by blending with an unknown species, as its observed wavelength differs from the Ritz value by about 0.009 Å. The identifications of the lines in the EIS list heavily rely on a comparison of the observed intensities with those produced by modeling with the CHIANTI database (Del Zanna et al. 2021) mentioned in Section 1.

Most of the lines newly identified by Landi & Young (2009) belong to the transitions from the levels of the $3p^5 3d^3$ $^5S°$, $^5D°$, and $^5F°$ terms to the ground configuration $3p^6 3d^2$. These transitions have very small radiative rates and are not seen in vacuum spark spectra, where the high electron density causes these levels to be depopulated by collisions. Special conditions of excitation in the solar plasma with its very low electron density also permitted the parity-forbidden $(3p^6)3d^2$ ^3F_J–$3d4s$ $^3D_{J'}$ transitions to be seen. They were first identified in EIS spectra by Brown et al. (2008) using Ritz wavelengths calculated from Fe VII energies of Ekberg (1981). It should be noted that the wavelengths of these lines coincide with those of the Fe VI lines of Ekberg (1975). However, the apparent absence of some other strong Fe VI lines shows that the Fe VI line blending is not significant in the EIS spectrum studied. We adopted the wavelengths derived from measurements of Landi & Young (2009). The measured wavelengths listed in that work are affected by a Doppler shift. To reduce them to the laboratory rest frame, we adopted the correction corresponding to a velocity of (-40.4 ± 4.5) km s^{-1} derived by Young & Landi (2009) from a large set of observed lines of different species. The systematic uncertainty of this correction, 4.5 km s^{-1}, was combined in quadrature with the statistical uncertainties given by Landi & Young (2009) to obtain the total uncertainties given in Table 2. For blended lines, the uncertainty was increased by a large fraction of the FWHM (depending on the difference of the observed and Ritz wavelengths). For lines that were measured solely by EIS, these same wavelengths and their uncertainties are given in Table 4 and were used in the level optimization.

Several questions have occurred concerning previous analyses of Fe VII spectral lines. We will discuss the identifications and address these questions below.

The level with $J = 1$ in the $3p^5(^2P°)3d^3(^2F)$ $^3D°_J$ term was not known. It was suggested by Young & Landi (2009) that the 189.36 Å line in the EIS spectrum (Landi & Young 2009) could be the strongest transition from this level, but the other transitions were blended or absent. This suggestion was confirmed by the observation of the 182.406 and 189.467 Å lines in our higher-resolution laboratory spectrum. These lines

correspond to the $^3F_2$–$^3D_1^\circ$ and $^3P_1$–$^3D_1^\circ$ transitions in the $3p^63d^2$–$3p^53d^3(^2F)$ sub-array. The 189.467 Å line is resolved from the stronger 189.450 Å line of the $^3P_1$–$^3D_2^\circ$ transition of the same sub-array, but its observed intensity can be over-estimated. It should be noted that in the laboratory spectrum, this line can have a contribution from an Fe VI line measured as 189.478 Å (Azarov et al. 1996).

Young & Landi (2009) noted that the $\lambda182.07/\lambda188.58$ ratio in the solar spectrum, related to the transitions from the $3p^5(^2P^\circ)3d^3(^2F)\,^3D_3^\circ$ level, is significantly discrepant with theory, which implies that the latter is in error. We identified a mistake in Tables 4 and 5 of Young & Landi (2009): in the ratios involving the $\lambda188.58$ Å line, an incorrect value of the solar intensity of this line was used, 56.7 instead of 72.6 observed in the EIS spectrum (Landi & Young 2009). Thus, the observed ratio was 0.32 ± 0.13 instead of the 0.407 ± 0.164 mentioned by Young & Landi (2009). The theoretical ratio referred to therein is 0.13 as calculated by Witthoeft & Badnell (2008), so the statement about discrepancy still stands. In our laboratory spectrum, the branching ratios for all transitions from this $^3D_3^\circ$ level at 551,567 cm^{-1} are in agreement with our calculated A values. In particular, the $\lambda182.07/\lambda188.58$ intensity ratio 0.37 observed in our spark spectrum is close to our calculated ratio of A values, 0.38. It should be noted that after correction for variation of sensitivity with wavelength and averaging over all experimental data (see Section 6), the ratio of reduced observed intensities is 0.41. It coincides with the ratio of our recommended A values (see Section 5).

The level at 553 223.3 cm^{-1} labeled by Young & Landi (2009) as $(b^2D)^1D^\circ$ was known from Ekberg (1981) as $3p^5(^2P^\circ)$ $3d^3(^2F)^1D^\circ$. In fact, as seen in Table 5, the wave function of this level consists of a close mixture of both LS terms: 24% $(^2F)^1D^\circ$ and 20% $(^2D1)^1D^\circ$, justifying Ekberg's assignment. The basis state with LS label $(^2D1)^1D^\circ$ is "dissolved" between experimental levels at 553,223.3 cm^{-1} and 539,427 cm^{-1} and some other unobserved levels.

Young & Landi (2009) predicted the $3p^63d^2\,^3P_1$–$3p^5$ $(^2P^\circ)3d^3(^4P)\,^3P_0^\circ$ line at 185.34 Å, but did not find it in the EIS spectrum possibly due to its blending with the strong Fe VIII line at 185.213 Å. This suggestion is supported by the 185.390 Å line well resolved from the Fe VIII line in our spectra. This line coincides in wavelength with a Fe VI line (Azarov et al. 1996), but the contribution of Fe VI to its intensity on our spectrograms is small.

Del Zanna (2009), independently from Young & Landi (2009), published a list of the so-called "cool lines" including Fe VII observed by Hinode EIS. He also measured and analyzed one of the plates taken by B. C. Fawcett (Fawcett & Cowan 1973) containing Fe VII lines. Only five lines from his list of the newly identified Fe VII lines were confirmed by our study, four of them being assigned to incorrect transitions.

Liang et al. (2009) studied spectra of iron excited in the Heidelberg electron beam ion trap (EBIT) with electron energies varied in 5 eV steps between 75 and 544 eV. The observed spectra show the evolution of each ionic stage from Fe VI to Fe XV as a function of the electron beam energy. This allowed those authors to distinguish emission lines from neighboring ion charge states. The spectra were recorded in the range from 125 to 265 Å with a resolution varying between 0.5 and 0.8 Å. It was suggested that some of the known Fe VII lines could belong to Fe VI. Our comments on these lines are given below.

Liang et al. (2009) observed that excitation of the line near 180.06 Å occurs at lower electron beam energies than those required to produce Fe^{6+} ions. It was already known from the work of Azarov et al. (1996) that there is a Fe VI line at 180.062 Å. Both in our spectrograms and those of Ekberg (1981), this line is about three times stronger than predicted in Fe VII. Thus, we marked it as blended by Fe VI in Table 4.

A similar observation was made by Liang et al. (2009) for the group of unresolved weak lines near 182.3 Å containing the lines at 182.221 and 182.406 Å first classified as Fe VII by Ekberg (1981). In our spectra, the 182.221 Å line is situated on the overlapping wings of two closely lying Fe VI lines at 182.202 and 182.240 Å (Azarov et al. 1996), thus preventing accurate measurements of its wavelength and intensity. We adopted Ekberg's wavelength and estimated the intensity relative to the 181.103 Å line. The line at 182.406 Å is on the far wing of the 182.382 Å Fe VI line (Azarov et al. 1996). Its observed intensity in the laboratory spark spectrum is in good agreement with our calculated transition rates. Possibly, the low signal-to-noise ratio prevented this transition to be observed in the low-resolution EBIT spectrum of Liang et al. (2009).

Liang et al. (2009) also reported an observation of three Fe VII lines at 127.3, 236.5, and 240.2 Å, which they described as previously unidentified but present in the solar spectrum observed by Malinovsky & Heroux (1973). It should be noted that, according to Ekberg (1981), the 127.3 Å line represents the unresolved $(3p^6)3d^2\,^3F$–$3d5f\,^3G^\circ$ multiplet, and the 240.2 Å line is the $3d^2\,^3P_2$–$3d4p\,^3P_2^\circ$ transition listed at 240.2236(15) Å in Table 4. The third line at 236.5 Å is present in our Fe VII analysis with the wavelength 236.4524(20) Å (see Table 4), but our identification differs from that of Liang et al. (2009).

Identifications of several other Fe VII lines in Ekberg (1981) were questioned by Beiersdorfer & Träbert (2018). They observed the iron spectra from an EBIT at the Lawrence Livermore National Laboratory running at the lowest electron beam energy of 200 eV. The spectra were recorded in the 165–175 Å range with a high spectral resolution of about 3000 (equivalent to $\approx$0.06 Å at $\lambda = 170$ Å, which is still about four times worse than in our spectra). They decided that six lines at 170.417, 170.565, 171.279, 171.530, 171.680, and 172.069 Å might not belong to Fe VII, and it is very likely that their identification is incorrect. After a careful check of observed and Ritz wavelengths and a comparison of measured branching ratios with the calculated ones, we can support the previous identifications of these lines by Ekberg (1981). However, a change of intensities with varying spark conditions shows that indeed, three of these lines at 170.565, 171.530, and 171.680 Å are blended by unknown lines of higher than Fe VII state of ionization. Thus, our observed intensities of these lines are larger than they would be in a clean Fe VII case.

And finally, all lines of the $(3p^6)3d4p$–$3d4d$ transition array from the analysis of Ekberg & Feldman (2003) are retained in Table 4 with several small changes. Our calculations did not confirm the addition of the $(3p^6)3d4p\,^3D_1^\circ$–$3d4d\,^3S_1$ classification to the 732.133 Å line (doubly identified by Ekberg & Feldman 2003). The labeling of the $(3p^6)3d4d\,J = 3$ levels at 556,345.7 and 556,084.2 cm^{-1} must be interchanged following the wave function compositions of Table 5. And the 741.134 Å line, although doubly classified, together with the two lines at 1166.301 and 1174.051 Å confirms the $3p^5(^2P^\circ)3d^3(^2P)\,^3P_2^\circ$ level at 430,202.3 cm^{-1}. As further discussed in Section 4, the

Table 6
Parameters of the Least-squares Fit of Fe VII Energy Levels with Cowan's Codes

Configurations		Parameter	LSF (cm^{-1})[a]	Δ (cm^{-1})[b]	Group[c]	HFR (cm^{-1})[a]	LSF/HFR[a]
Even parity							
$3p^63d^2$		E_{av}	34719.4	37		0.0	
$3p^63d^2$		$F^2(3d, 3d)$	110296.6	266	3	119,686.588	0.9215
$3p^63d^2$		$F^4(3d, 3d)$	73729.5	275	5	75,965.882	0.9706
$3p^63d^2$		α_{3d}	−60.6	8	8	0.0	
$3p^63d^2$		β_{3d}	−812.5	104	9	0.0	
$3p^63d^2$		T_{3d}	0.0	fixed		0.0	
$3p^63d^2$		ζ_{3d}	634.5	20	1	662.3	0.9580
$3p^63d4s$		E_{av}	373,660.4	49		334,325.3	1.1177
$3p^63d4s$		ζ_{3d}	685.8	21	1	715.8	0.9581
$3p^63d4s$		$G^2(3d, 4s)$	11,988.3	292	2	13,365.882	0.8969
$3p^63d4d$		E_{av}	587,998.1	26		550,614.1	1.0679
$3p^63d4d$		ζ_{3d}	689.7	21	1	719.9	0.9580
$3p^63d4d$		ζ_{4d}	135.6	4	1	141.5	0.9583
$3p^63d4d$		$F^1(3d, 4d)$	−458.9	250		0.0	
$3p^63d4d$		$F^2(3d, 4d)$	24,703.6	238	4	28,645.059	0.8624
$3p^63d4d$		$F^4(3d, 4d)$	12870.3	331	6	13698.941	0.9395
$3p^63d4d$		$G^0(3d, 4d)$	8313.4	31	7	11,808.118	0.7040
$3p^63d4d$		$G^2(3d, 4d)$	10,463.7	236	10	12,146.235	0.8615
$3p^63d4d$		$G^4(3d, 4d)$	7160.0	359	11	9130.941	0.7841
Odd parity							
$3p^63d4p$		E_{av}	436,427.3	181		420,375	1.0382
$3p^63d4p$		ζ_{3d}	743.0	41	7	716.9	1.0364
$3p^63d4p$		ζ_{4p}	1695.7	42	21	1729.1	0.9807
$3p^63d4p$		$F^2(3d, 4p)$	30,673.6	1073	5	34,208.0	0.8967
$3p^63d4p$		$G^1(3d, 4p)$	10,688.8	680	15	11,225.882	0.9522
$3p^63d4p$		$G^3(3d, 4p)$	9310.5	909	16	10,970.353	0.8487
$3p^63d4p$	$3p^53d^3$	$R_d^1(3p, 4p; 3d, 3d)$	13,033.3	1087	22	12,236.5	1.0651
$3p^63d4p$	$3p^53d^3$	$R_d^1(3p, 4p; 3d, 3d)$	13,160.8	1097	22	12,356.2	1.0651

Notes.
[a] Parameter values determined in the ab initio pseudorelativistic Hartree–Fock (HFR) and least-squares-fitted (LSF) calculations and their ratio.
[b] Standard deviation of the fitted parameter.
[c] Parameters in each numbered group were linked together with their ratio fixed at the HFR level.

(This table is available in its entirety in machine-readable form.)

leading component of the wave function of this level is $3p^63d4p$ $^3D_2^\circ$ contributing 29% to its composition. Our calculations reveal that the main lines with the largest transition probabilities are absent in the identified transition arrays of three $3p^63d4d$ levels. This suggests that line identifications of the $(3p^6)3d4p$–$3d4d$ transitions need to be revisited. The levels in question are $^3D_3$ at 556 345.7 cm^{-1} with the strongest line missing at 841.824 Å, $^3G_4$ at 557,044.8 cm^{-1} with the two strongest lines missing at 802.022 and 793.032 Å, and $^3G_5$ at 558,228.7 cm^{-1} with the two strongest lines missing at 788.806 and 750.539 Å.

4. Theoretical Interpretation

For the final analysis, we extended the initial calculation described in Section 3. The following set of even-parity configurations was included in the calculation: [Ne]$3s^23p^6$ ($3d^2 + 3d4s + 3d4d + 3d5s + 3d5d + 4s^2 + 4s4d + 4p^2$), $3s3p^63d^3$, $3s^23p^53d^24p$, $3s^23p^4$ ($3d^4 + 3d^34s + 3d^34d$), and $3p^63d^4$. For the odd parity, the configuration interaction space consisted of the [Ne]$3s^23p^6$[$3dnp + 3dnf + 4snp + 4snf + 4dnp + 4dnf$ ($n =$ 4 to 10)], $3s^23p^5(3d^3 + 3d^24s + 3d^24d + 3d4s^2)$, $3s3p^53d^4$, and $3s^23p^33d^5$ configurations.

The optimized energy levels from Table 5 were used in the least-squares fitted (LSF) parametric calculations with Cowan's code (Cowan 1981; Kramida 2019). The LSF energy parameters

obtained in the fitting of all available Fe VII levels are displayed in Table 6 together with the corresponding relativistic Hartree–Fock (HFR) values and their ratios LSF/HFR (scaling factors). Some parameters were varied in groups, so that their ratios within each group remained fixed at the HFR values. The electrostatic parameters were scaled by 0.85, and spin–orbit parameters were taken at HFR values in the configurations with unknown levels. Most of the configuration interaction (CI) parameters were kept fixed at 0.85 scaling. In particular, all CI parameters of the even-parity system were kept fixed. However, the parameters for the interactions of $3s^23p^53d^3$ with $3s^23p^63dnp$ ($n = 4$ to 10) and $(3s3p^53d^4 + 3p^33d^5)$, $(3s^23p^5)(3d^3 + 3d^24s + 3d^24d)$ with $3s^23p^63dnf$ ($n = 4$ to 10), and all CI parameters within the $3s^23p^63dnf$ series were varied. At the last stages of the LSF, to improve the fitting, we introduced the effective parameters of illegal rank, such as $F^1(3d, 4d)$ of $3s^23p^63d4d$ in the even parity, as well as $F^1(3p, 3d)$ and $G^2(3p, nd)$ ($n = 3, 4$) of the odd-parity complex $3s^23p^5(3d^3 + 3d^24s + 3d4s^2 + 3d^24d) + 3s3p^53d^4 + 3s^23p^33d^5$. The standard deviation of the fitting, σ (computed a posteriori, see below), was 144 and 388 cm^{-1}, respectively, for the even and odd level systems. Differences of observed energies from those calculated in the LSF are included in Table 5. The three leading eigenvector components (in LS coupling) are also specified along with their percentages, where the latter exceeds 5%.

In the following discussion, for better readability, we again omit the labels of completely filled electronic subshells up to $3s^2$ from the level designations.

For the $3p^53d^24s$ configuration, Ekberg (1981) used a peculiar angular momentum summation scheme in which the outer $4s$ electron was first combined with $3d^2$, producing intermediate even-parity doublet and quartet LS terms. Then these terms were combined with the $^2P°$ term of the $3p^5$ subshell to produce the final singlet, triplet, and quintet LS terms of odd parity. Ekberg's level designations were used in the compilation of Sugar & Corliss (1985), which was the basis of the current data set in the NIST ASD (Kramida et al. 2020). We calculated the eigenvector compositions in this coupling scheme and compared it with the usual scheme of sequential addition of subshells with increasing principal and orbital quantum numbers. That is, in the traditional sequential LS coupling, the angular momenta of the $3p^5$ and $3d^2$ subshells are combined first, producing doublet and quartet intermediate LS terms of odd parity. Then these intermediate terms are combined with the ^1S term of the outer $4s$ electron to produce the same set of final LS terms. It turned out that the traditional sequential LS coupling gives a slightly better purity of the eigenvectors, i.e., the average leading percentage is 65% in Ekberg's coupling and 69% in traditional sequential coupling. Therefore, the latter is chosen for designating the $3p^53d^24s$ levels in Table 5.

It can be seen in Table 5 that the leading wave function components of many levels have percentages less that 50%. In cases when the first component is less than about 40%, the second one can have a comparable or even the same value, as, for example, in the $3p^53d^3$ level at 424,628.7 cm^{-1} with the first component 18% $3p^5(^2P°)3d^3(^2D2)$ $^3D_2°$ and the second one 18% $3p^63d4p$ $^3D_2°$. The wave function composition in such cases strongly depends on the atomic model adopted in the calculations. A direct consequence of the wave function mixtures is an ambiguity in characterization of a level by a single-term label, which is a common practice in most atomic structure computer codes. It explains the different designation of some levels in comparison with Ekberg (1981). It is also very often that two levels possess the same term as the leading component. Sometimes even three levels have the same term as the leading component. For example, in our initial calculation with the smaller configuration sets described in Section 3, among the odd-parity levels with $J = 3$, the $3p^63d4p$ $^3D°$ term was the leading one for the three levels at 425,249.5, 430,946.5, and 431,608.5 cm^{-1}. In the final extended calculation, the leading component of the level at 425,249.5 cm^{-1} became $3p^5(^2P°)3d^3(^2D2)$ $^3D°$ (see Table 5). We found it possible to disentangle the level labels by manually moving some minor component (in most cases, the second one) to the first place. The most extreme example is the level at 430,202.4 cm^{-1} ($J = 2$), where the fourth component contributing only 7% to the eigenvector had to be used to label the level as $3p^5(^2P°)3d^3(^2P)$ $^3P°$, since the first, second, and third components had already been used to label other levels (see more about this level below). Designating a level by a term label of the third or fourth component with about 10% contribution has little physical meaning. Therefore, we designated the levels in Table 4 by their sequential numbers defined in Table 5 to have an unambiguous relation between these two tables.

All of the levels established by Ekberg (1981), except for $(a^2D)^1D_2$ at 538,290 cm^{-1} discussed above, were confirmed. One special case is related to Ekberg's $3p^63d4p$ $^3F_2°$ level at 430,213.4 cm^{-1}. In our analysis, it is split into two $J = 2$ levels

at 430,211.2 cm^{-1} and 430,202.4 cm^{-1}. The first one has 65% of $3p^63d4p$ $^3F°$ in its composition, while the second one is strongly mixed: 29% $3p^63d4p$ $^3D°$ + 18% $3p^63d4p$ $^3F°$ + 10% $3p^5(^2P°)3d^3(4F)$ $^3D°$; it has been designated as $3p^5(^2P°)3d^3(^2P)$ $^3P°$, which is the fourth component of its composition with a contribution of 7%.

The order of the calculated eigenvalues within each group of the same J value and parity differs from that established experimentally. This is easy to detect when the levels are almost pure in LS coupling. It is more difficult when the levels are strongly mixed. In such cases, the correspondence between experimental and theoretical levels can be established using the patterns of intensities of observed and predicted lines from the levels in question. This method has been explained by Kramida (2013). We used this method to correct errors in a few of our assignments of experimental levels used in the LSF. This correction can only be made after the calculation of radiative transition probabilities. Since the calculations are fairly large, we decided not to repeat them with the corrected level assignments. Thus, the standard deviations σ of the LSF specified at the beginning of this Section have been computed a posteriori, i.e., after the corrections were made to the level assignments. Similar errors in level assignments have been found in the data calculated by Kurucz (2010) and by Li et al. (2018). For example, the odd-parity levels at 430,946.5 and 431,608.5 cm^{-1} with $J = 3$ have been interchanged in the tables of those authors, as well as in our extended LSF. Their assignment was correct in our initial LSF with a reduced set of configurations, since it was made in the analysis with the IDEN2 visual identification code (Azarov et al. 2018). This type of analysis heavily relies on the patterns of observed and predicted line intensities, which makes the level assignments much more dependable.

As mentioned above, problems with establishing correspondence between experimental and theoretical levels are common to many published calculations of Fe VII properties. As demonstrated by Zeng et al. (2005), the calculated energy structure and transition rates strongly depend on the extent of account for CI effects. Those authors included in their ab initio calculations a set of interacting configurations that was similar to the present analysis, giving rise to 1949 fine-structure levels in total (it was 1250 in the present calculation). Nevertheless, their calculated energy levels are in error by about 15,000 cm^{-1} on average, and the order of the calculated energies differs from that observed in experiments. Combined with the fact that all of their calculations were made in the jj coupling scheme, while all observed levels are classified in LS coupling, this explains several errors in their assignments of experimental levels to the theoretical ones. These calculations were used in the work of Liang et al. (2009), to which those errors have propagated.

While the basis set used in our LSF calculation is necessarily smaller than in most published ab initio calculations, the LSF drastically improves the accuracy of the calculated energies and transition rates due to the semiempirical adjustment of the Slater parameters. A comparable improvement of ab initio results requires a tremendous increase in the volume of the CI included. For example, Li et al. (2018) have included about 8,000,000 configuration state functions (equivalent to the number of fine-structure levels) in their calculations. As a result, the rms difference of their calculated energies from experiments is about 3000 cm^{-1}. This is much better than that in the calculations of Zeng et al. (2005), as well as in other calculations of a comparable size (Witthoeft & Badnell 2008;

Tayal & Zatsarinny 2014). The difference from experiments is still an order of magnitude greater than that in our LSF, and some theoretical levels were wrongly associated with experimental ones.

5. Transition Probabilities

As mentioned in Section 1, the last time a critical assessment of published data on radiative transition probabilities (A values) was made for Fe VII was 1988, when the critical compilation of Fuhr et al. (1988) was published. The data included in the current version of the NIST ASD (Kramida et al. 2020) are from this compilation, and it is easy to see that most of the 144 available A values were assigned accuracy codes D ($\leqslant 50\%$) and E ($>50\%$). It is reasonable to expect that the modern calculations mentioned in the previous Section have produced much more accurate results.

We begin the assessment with forbidden transitions between the levels of the ground configuration $3p^6 3d^2$. The old calculation of Nussbaumer & Storey (1982), from which the A values of Fuhr et al. (1988) were quoted, was made with the SUPERSTRUCTURE code of Eissner et al. (1974). This code is in principle similar to that of Cowan, as it uses a nonrelativistic calculation with hydrogenic wave functions and with relativistic corrections and CI added as perturbations. Moreover, the calculation of Nussbaumer & Storey (1982) was not ab initio: they used empirical adjustment terms in the matrix of the electrostatic interaction, which ensured correct term positions, as well as some adjustable parameters of the Thomas–Fermi and hydrogenic potentials used in the calculation of radial wave functions of configurations with principal quantum numbers $n \leqslant 3$ and $n \geqslant 4$, respectively. As a result, the calculated fine-structure separations within the ground configuration agreed with the experimental ones within less than $50\,\mathrm{cm}^{-1}$, which is eight times better than the corresponding data of Li et al. (2018), but four times worse than our present LSF. Nussbaumer & Storey (1982) had included 17 configurations in their CI complex, which is even greater than in our LSF (14 configurations of even parity). Thus, one should expect their wave functions to be quite accurate, as well as the M1 transition probabilities, which depend only on the wave functions.

Another set of M1 and E2 A values was calculated by Kurucz (2010) using a different version of Cowan's code and a different set of 61 interacting configurations, which included many highly excited $3p^6(3d + 4s)nl$ ($l = s, d, g, i$) configurations not included by us or by Nussbaumer & Storey (1982). Despite this difference in the size of the basis set, Kurucz's calculation is similar to ours and to that of Nussbaumer & Storey (1982) in the use of a nonrelativistic code with relativistic corrections and superposition of configurations. This method is very different from the fully relativistic multi-configuration calculation of Li et al. (2018), in which the radial wave functions of each subshell were adjusted in the self-consistent field calculation.

Figure 3 compares our M1 and E2 A values with those of Nussbaumer & Storey (1982), Li et al. (2018), and Kurucz (2010). The error bars in these figures represent the internal uncertainties of our A values, which have been evaluated using the Monte Carlo technique described by Kramida (2014b).

To avoid additional errors in A values caused by inaccuracy of the calculated transition energies, Figure 3 plots the ratios of line strengths S instead of A values.

From Figure 3(a) one can see that these four very different calculations agree almost perfectly for the strongest M1 transitions with line strengths greater than 1 a.u. (atomic units). For weaker transitions, the discrepancies grow, especially for the calculation of Li et al. (2018). This does not necessarily mean that this calculation had greater errors: the good agreement between the other three calculations can be explained by the similarity of these three calculations discussed above. A similar picture is seen for the E2 transitions in Figure 3(b). In both cases, the results of Nussbaumer & Storey (1982) are in the middle of the other three for most transitions. Thus, we adopted the old results of Nussbaumer & Storey (1982) with uncertainties evaluated from the spread of discrepancies between the other results for a few ranges of line strength S. These uncertainties turned out to be much smaller than those adopted by Fuhr et al. (1988) for most transitions.

A similar comparison for the $(3p^6)3d^2–3d4s$ transitions is shown in Figures 3(c) and (d) for M1 and E2 transitions, respectively. For both types of transitions, discrepancies between different calculations are much larger in this case. For M1 transitions (Figure 3(c)), they exceed six orders of magnitude for some transitions, while for E2 transitions (Figure 3(d)), some of the discrepancies reach almost ten orders of magnitude. The M1 contribution is extremely small in most of these transitions, so discrepancies in its magnitude are of little consequence for the total transition rates. However, they are troubling, since the calculation of M1 transition rates depends only on the quality of wave functions. It is unclear whether the wave functions of Li et al. (2018) or those of the two Cowan-code calculations are in error here.

For the much stronger E2 transitions, our calculation is unexpectedly very close to that of Li et al. (2018), while Kurucz's A values are smaller by three to almost 10 orders of magnitude (see Figure 3(d)). For these transitions, we adopted the results of Li et al. (2018). The uncertainties assigned to them in Table 4 have been evaluated from the discrepancies with our A values. Kurucz's results were discarded as erroneous. Most probably, the large errors in his calculation were caused by omission of many configurations involving excitations from the $3s$ and $3p$ subshells, which were included in both our calculation and that of Li et al. (2018).

Now we turn to an estimation of uncertainties for electric dipole (E1) transitions. This estimation is illustrated in Figure 4. The only means of estimation of uncertainties provided in the data set of Li et al. (2018) is the so-called uncertainty indicator dT, which was defined following Ekman et al. (2014) as

$$dT = \frac{|A_l - A_v|}{\max(A_l, A_v)}, \tag{2}$$

where A_l and A_v are the A values computed in the length and velocity forms, respectively.

It should be noted that dT as defined by Equation (2) always underestimates the uncertainty. This follows from the use of max in the denominator of this equation. Statistically, in the absence of systematic discrepancy, half of the A_l values are smaller than A_v, and half are greater. The smaller of the two values is always replaced by the greater one, decreasing dT and making its upper bound to equal unity. Another drawback of using dT is that it destroys information about the actual value of A_v, which can be useful in some cases.
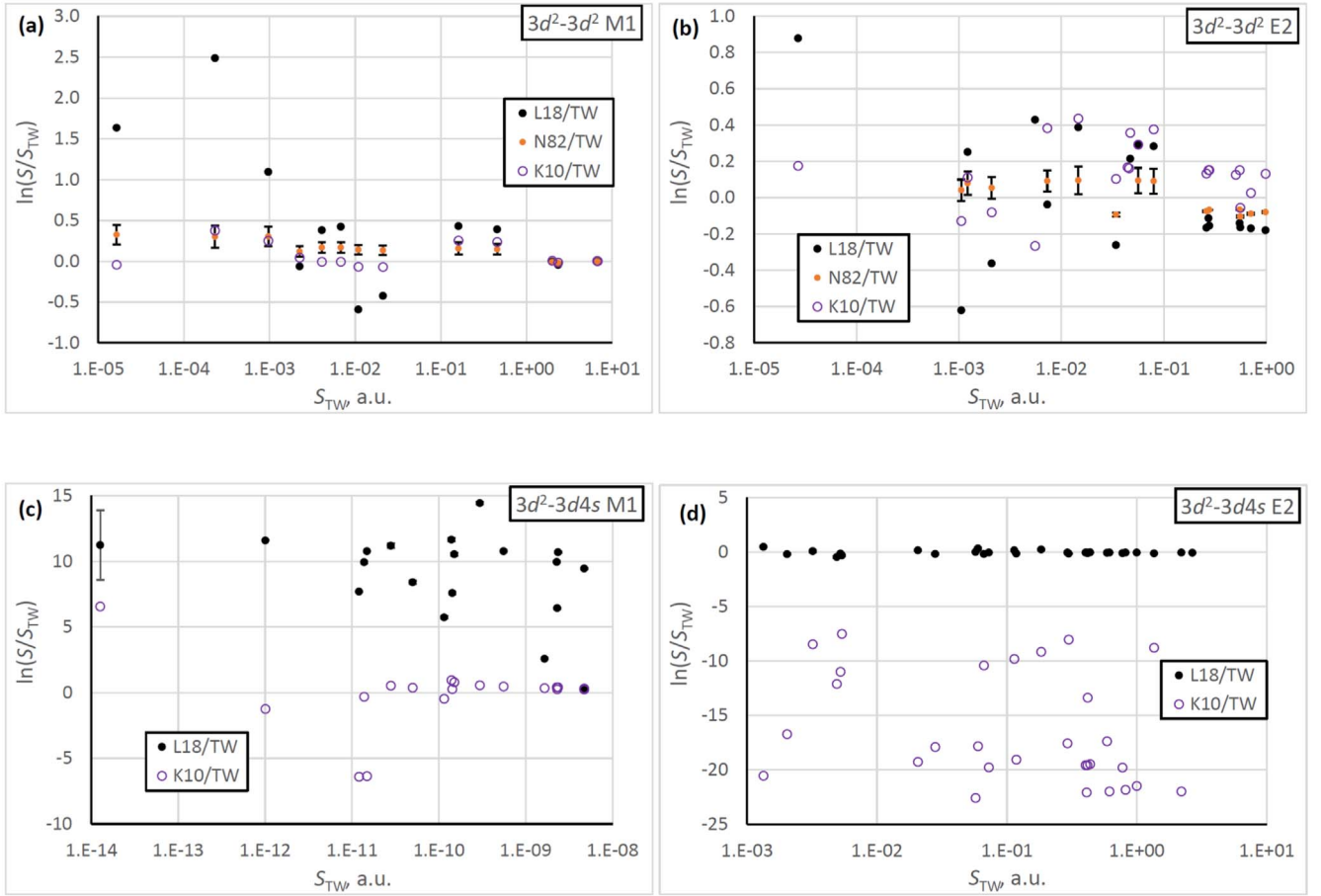
Figure 3. Comparison of transition line strengths for forbidden M1 and E2 transitions within the ground configuration $3p^6 3d^2$ (a, b) and between the ground configuration and $3p^6 3d4s$ (c, d) of Fe VII calculated in the present work (TW) with those of Nussbaumer & Storey (1982, N82), Li et al. (2018, L18), and Kurucz (2010, K10). The error bars represent the internal uncertainties of our calculation assessed with Monte Carlo random trials (Kramida 2014b). Note that the quantity on vertical axes is the *natural* logarithm of the ratio S/S_{TW} approximately equal to $2.3\log_{10}(S/S_{TW})$.

Instead of using this estimator, we use another quantity defined as

$$dS = \ln(S_1/S_2) \quad (3)$$

to compare any two results S_1 and S_2 for the line strength of a certain transition. When the differences between the two calculations are small, both Equations (2) and (3) give the same result. However, Equation (3) eliminates the errors in transition energies from the compared values. It also gives a more robust estimate of discrepancies when the accuracy is poor.

Unfortunately, this is the case here. We stress again that Figures 3 and 4 compare the results of the very best calculations ever performed for Fe VII. Nevertheless, both figures show very large discrepancies between these calculations, especially for weak transitions.

From Figure 4(a), the A values of Li et al. (2018) are expected to be accurate to about 10% for transitions with line strength $S > 0.1$ a.u. However, a comparison with the present results in Figure 4(b) shows a much larger disagreement for some of the strongest transitions. Panel (c) of the same figure allows estimation of internal uncertainties of the present calculation by comparing its results with those of a smaller calculation made with the same method (in this case, with our initial LSF described in Section 3). There are relatively few very large differences: for 38 transitions out of a total 499 depicted in panel (c), the quantity dS is large, $dS > 1$,

corresponding to ratios of a factor of three or greater. If these few outliers are excluded, the rms value of dS for the rest of the transitions is 0.27. This corresponds to an average difference of about 31%.

Figure 4(d) compares our calculation with that of Kurucz (2010). This plot shows a particularly regular shape: the scatter of points increases with decreasing line strength. Panels (b) and (d) show a very similar level of agreement between our calculation and those of Li et al. (2018) and Kurucz (2010). If 8% of transitions with the largest deviations are discarded (similar to what was done above for panel (c)), the rms of dS for the remaining transitions is about 0.4 for both panels (b) and (d). This corresponds to average differences of about 50%.

An initial estimation of the uncertainties of each calculation was made with the method described in Kramida (2013), i.e., by calculating the rms of dS in some bins in the range of S. Transitions for which the discrepancies $|dS|$ between different calculations exceeded the rms value were assigned larger uncertainties corresponding to the actual values of $|dS|$. Then these initial estimates were checked by comparison of calculated and observed line intensities. Although the observed intensities may be affected by various uncontrollable factors, such as self-absorption or resonance population transfer, they usually correspond within a factor of two or three to predictions of a simple model (see Section 6). Larger discrepancies between calculated and observed intensities indicate that the calculated A value may
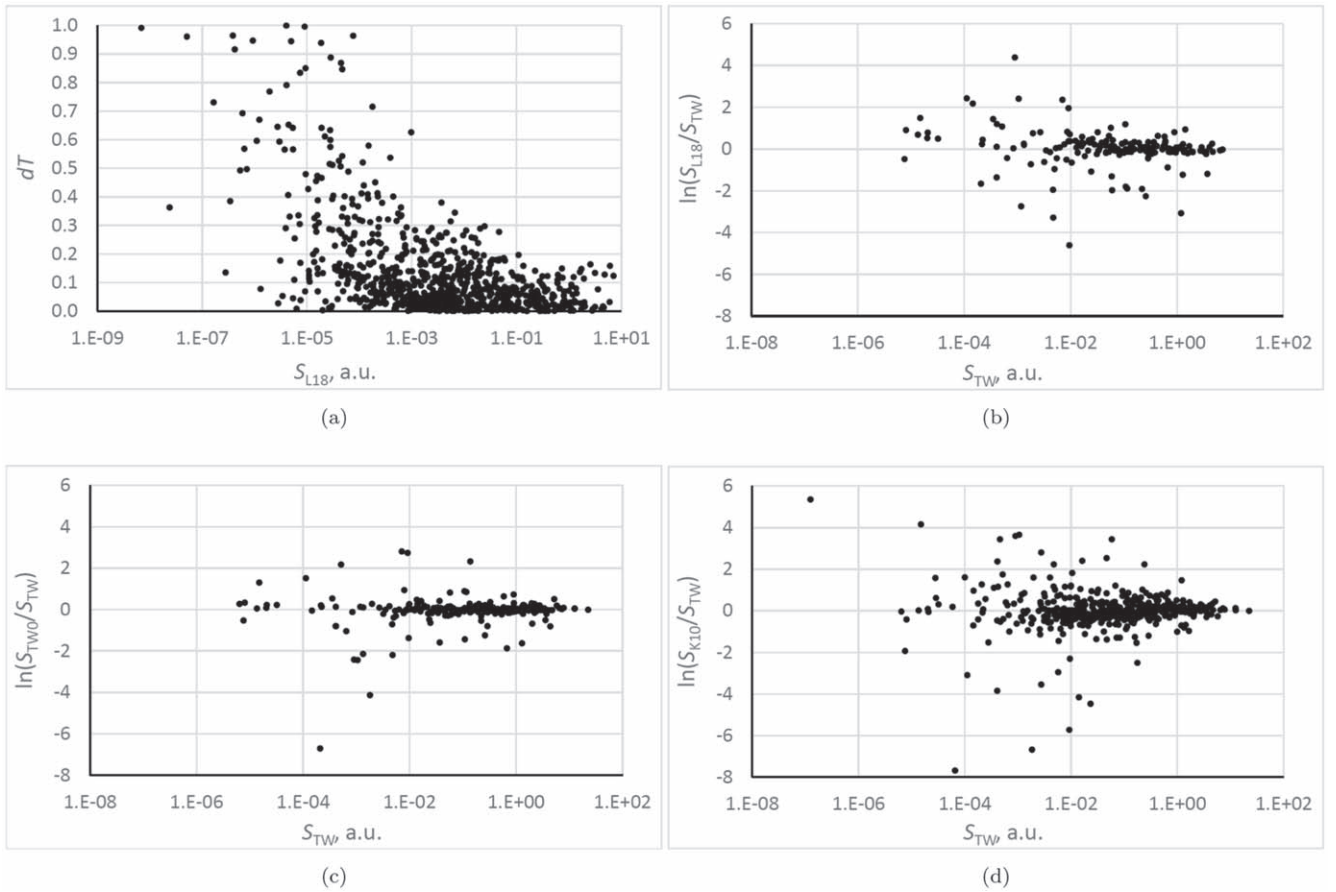
Figure 4. Estimation of uncertainties of calculated *A* values of internal uncertainties of allowed (E1) transitions of Fe VII. (a) Values of uncertainty indicator *dT* (see the text) illustrating internal uncertainties of calculations of Li et al. (2018, L18). (b)–(d) Comparison of transition line strengths calculated in the present work (TW) with those of L18, initial calculations of the present work (TW0), and Kurucz (2010, K10).

have a large error, and the uncertainty estimates have been degraded in such cases. On the other hand, for some transitions, the *dS* values for all calculations compared were consistently smaller than the rms values. For such transitions, the uncertainty estimates were upgraded to the smaller values. In each case, for the final data set, we selected the results of the calculation having the smallest estimated uncertainty. The selected *gA* values are given in Table 4 for each transition together with an accuracy code following the convention of the NIST ASD (Kramida et al. 2020).

6. Observed Line Intensities

The observed line intensities have been analyzed using the method described by Kramida (2013). Reduction of line intensities observed in the present work to a common uniform scale is illustrated in Figure 5.

The base of the common scale for all line intensities was established from our observations made on imaging plates in the grazing incidence region (158–266 Å). Although the imaging plates are known to have a nearly linear response to exposure in a wide dynamic range, their sensitivity varies with wavelength. In addition, reflectivity of the diffraction grating of the spectrometer also varies with wavelength. The exact dependence of the total sensitivity of our setup on wavelength is unknown. However, it can be established approximately from a comparison of observed and calculated intensities, as explained below (following Kramida 2013).

Under the conditions of local thermodynamic equilibrium (LTE), the intensity *I* of an emission line (in terms of total energy flux under the line's spectral profile) is given by the Boltzmann formula,

$$I = C\frac{gA}{\lambda}\exp\left(-\frac{E_{\rm up}}{T_{\rm eff}}\right), \qquad (4)$$

where $E_{\rm up}$ is the energy of the upper level of the transition, $T_{\rm eff}$ is effective excitation temperature, $g = 2J + 1$ is statistical weight of the upper level, *A* is the spontaneous radiative decay rate, and *C* is a coefficient depending on the population of the ground level of the ion and on the units in which *I* is measured.

First, we calculate the Boltzmann factors as

$$B = \ln\left(\frac{I_{\rm obs}\lambda}{gA}\right), \qquad (5)$$

where $I_{\rm obs}$ is the observed intensity (in arbitrary units on a linear scale with regard to exposure). The argument of the natural logarithm represents a quantity proportional to the level population.

The Boltzmann factors calculated for our imaging plate intensities in the grazing incidence region are plotted against $E_{\rm up}$ in Figure 5(a). The dotted line represents a linear fit. From Equation (4), its slope is equal to $1/T_{\rm eff}$. The linearity of the Boltzmann plot can be perfect only if several conditions are satisfied: (1) The level populations exactly follow the Boltzmann
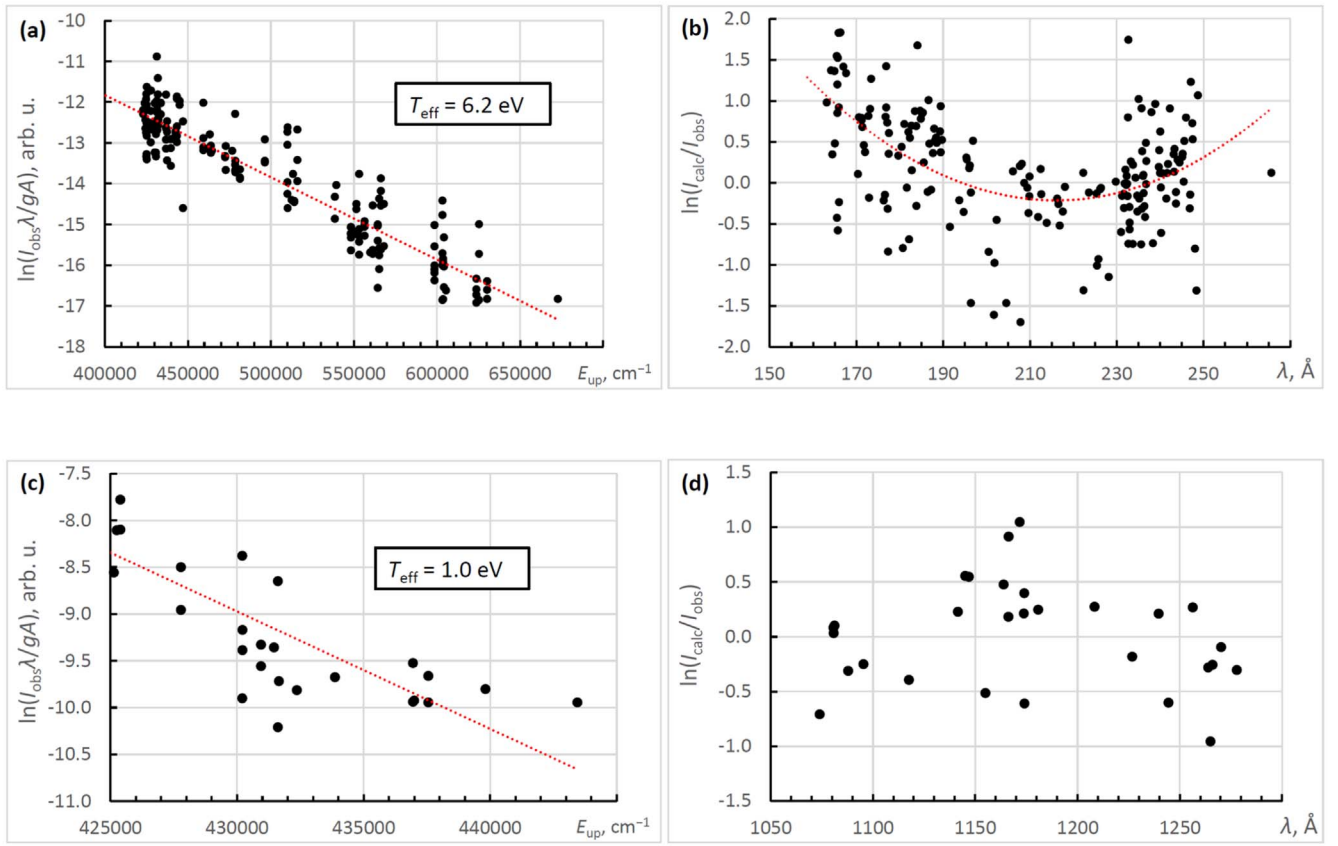
Figure 5. Reduction of line intensities observed in the present work. Panels (a) and (c): Boltzmann plots for the grazing and normal incidence regions, respectively. Panels (b) and (d): inverse logarithmic response functions for the grazing and normal incidence regions, respectively.

distribution; (2) The plasma is optically thin for all transitions; (3) All of the A values are exact; (4) The observed intensities are not affected by blending, and all transitions are correctly identified; and (5) The wavelength-dependent variations of sensitivity are removed from the observed intensities. In most laboratory settings, it is very difficult or impossible to satisfy all of these conditions. However, their influence can be reduced to some extent. With a large number of observed lines, it is usually easy to detect transitions with especially poorly calculated A values. A majority of them are weak lines, for which calculations are likely to be affected by cancellation effects. Such lines are excluded from the plots.

If the linear fit of the Boltzmann plot is expressed as $-aE_{up} + b$, then $T_{eff} = 1/a$ (in the same units as E_{up}), and the value of the coefficient C of Equation (4) can be inferred as $C = \exp(b)$. Then, the predicted intensities I_{calc} can be calculated by Equation (4). The next step is to find the wavelength-dependent response function of the instrument. In this work, we use the inverse logarithmic response function $R(\lambda)$ defined as follows:

$$I_{corr} = I_{obs} \exp[R(\lambda)], \qquad (6)$$

where I_{corr} is the corrected intensity. In most experiments, $R(\lambda)$ is smooth (or at least contiguous) and can be approximated by a polynomial. In the subsequent text and figures, it is called "response function" for brevity.

The function $R(\lambda)$ can be found by plotting the natural logarithm of the ratio I_{calc}/I_{obs} against wavelength, as shown in Figure 5(b). In this panel, $R(\lambda)$ is fitted by a parabola, shown as the dotted curve. The calculation proceeds iteratively: all values

of I_{obs} in Equation (5) are replaced with I_{corr} of Equation (6), and the cycle repeats until the T_{eff} value determined from the Boltzmann plot stops changing. For this process to converge, the range of excitation energies E_{up} must be sufficiently large and the data scatter sufficiently small, so that the linear fit of the Boltzmann plot would be statistically justified. There are also some limitations on the sets of transitions in the data. For example, if all observed transitions represent one Rydberg series, it is impossible to simultaneously fit both T_{eff} and $R(\lambda)$ from these plots. In our case, the process converged with $T_{eff} \approx 6.2$ eV. Figure 5 shows the results of this converged fitting, so the quantity I_{obs} on the vertical axis of panel (a) actually represents the corrected intensities I_{corr}. The accuracy of T_{eff} is determined mainly by the scatter of the data points in the Boltzmann plot; in this case, it is about 20%. The set of the corrected intensities I_{corr} for our grazing incidence imaging plates formed the basis of our global intensity scale. Intensities observed in all other laboratory experiments have been reduced to this scale as explained below.

In the normal incidence region, we used photographic plates to record the spectrum. The Boltzmann plot of these intensities is depicted in Figure 5(c). The effective temperature determined from this plot is significantly lower, $T_{eff} \approx 1.0$ eV. The response function illustrated by the plot in panel (d) is essentially flat: the scatter of the data points does not allow a linear or polynomial fitting with any level of confidence. This corresponds to $R(\lambda) \approx 0$, i.e., no intensity correction was applied.

The scale of our intensities in the photographic region is different from that of the imaging plates, and the effective
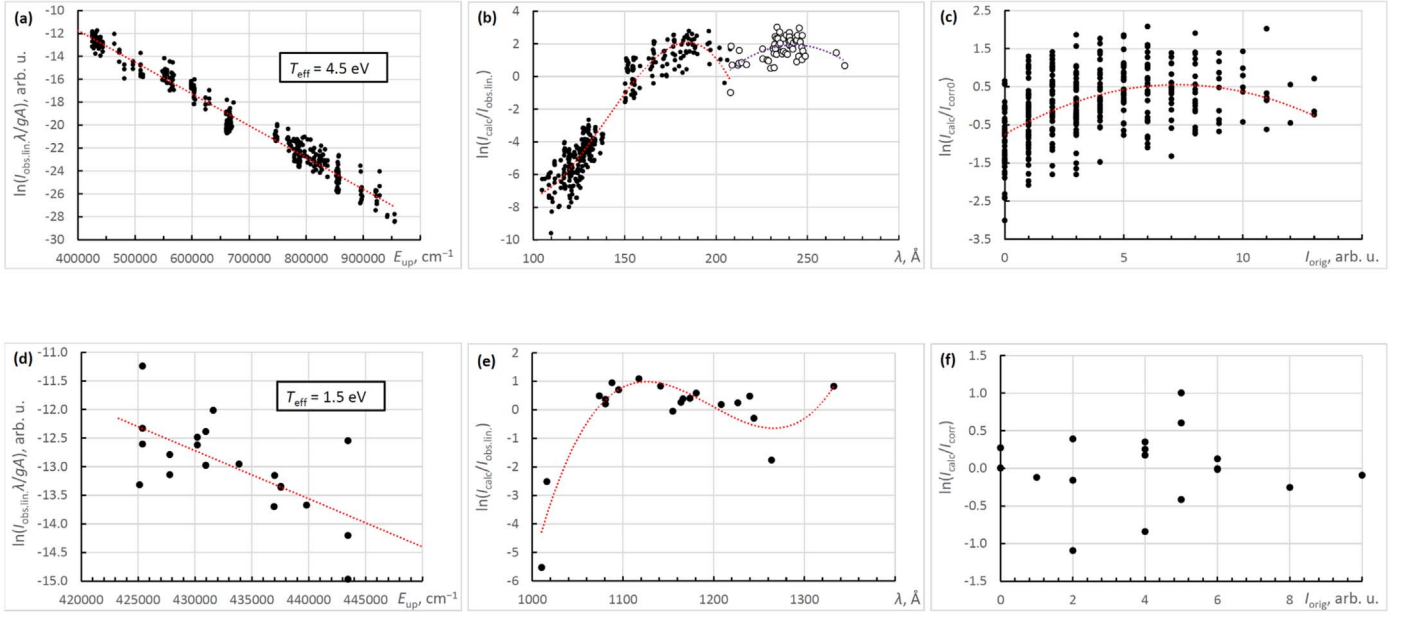
Figure 6. Reduction of line intensities observed by Ekberg (1981). Panels (a) and (d): Boltzmann plots for the grazing and normal incidence regions, respectively. Panels (b) and (e): inverse logarithmic response functions for the grazing and normal incidence regions, respectively. Panels (c) and (f): nonlinearity with respect to exposure for the grazing and normal incidence regions, respectively.

temperature is different. To reduce the photographic intensities to the scale of the imaging plates, we use the fitting coefficients of the two Boltzmann plots of Figures 5(a) and (c), respectively:

$$B_{\text{base}} = -a_{\text{base}} E_{\text{up}} + b_{\text{base}}, \quad B_1 = -a_1 E_{\text{up}} + b_1, \quad (7)$$

where the subscripts "base" and "1" correspond to the imaging plates establishing the base scale and the photographic plates, respectively. The photographic intensities reduced to the base scale, I_{reduced}, are then determined as

$$I_{\text{reduced}} = I_{\text{corr},1} \exp[-a_{\text{base}} E_{\text{up}} + b_{\text{base}} - (-a_1 E_{\text{up}} + b_1)], \quad (8)$$

where $I_{\text{corr},1}$ represents the corrected intensities of the data set being reduced (in this case, since $R(\lambda) = 0$, $I_{\text{corr},1} = I_{\text{obs}}$).

In principle, it is known that the response of photographic plates to exposure is nonlinear, especially for lines with strong blackening of the plate. Then, for bringing the intensities to a scale linear with regard to exposure, it becomes necessary to determine this nonlinearity and remove it from the corrected intensities. This can be done by plotting $\ln(I_{\text{calc}}/I_{\text{corr}})$ against the original observed intensities I_{obs} and fitting it by a smooth function. However, our values of I_{obs} did not show any statistically significant nonlinear dependence on exposure, so this correction was not necessary. Nevertheless, it was significant in the case of the photographic intensities reported by Ekberg (1981).

The study of Ekberg (1981) was similar to ours in the division of the observed lines into two regions, one in the grazing incidence region (short wavelengths below 271 Å) and the other in the normal incidence region (long wavelengths above 1010 Å). However, all his measurements were made on photographic plates of various types, and his line intensities were reported on a scale from 0 to 13. As we know from other works of Ekberg from this time period, these values were given on a logarithmic scale. Empirically, we found that the base of

this scale was different in the two spectral regions: about 1.5 in the grazing incidence region and 1.23 in the normal incidence region. Thus, prior to drawing the Boltzmann plots and response functions, the original reported intensities were roughly linearized as $I_{\text{obs.lin.}} = b_{\text{log}}^{I_{\text{obs}}}$, where the bases of the logarithm b_{log} were 1.5 and 1.23 in the two regions, as mentioned above. In the grazing incidence region, the inverse response function $R(\lambda)$ showed a narrow dip near 210 Å corresponding to an increase of sensitivity roughly by a factor of three compared to wavelengths of 180 and 240 Å (see Figure 6(b)). This apparent increase of sensitivity might be due to a local deviation of photographic emulsion density in this region of the spectrum. Such features are not uncommon in photographic spectrograms. In other cases, local peaks or sharp drops in spectral sensitivity curves may be caused by use of optical filters or by contamination of optics with oil or other materials used in the spectrographs. Such features may require fitting with peak functions. In the case shown in Figure 6(b), a piece-wise fitting with two different second-degree polynomials was adequate. The effective excitation temperature found from the Boltzmann plots was 4.5 eV for the grazing incidence region and 1.5 eV for the normal incidence region.

In the short-wavelength region, it was found necessary to correct the observed intensities for nonlinearity with respect to exposure. As mentioned above, it was done by plotting $\ln(I_{\text{calc}}/I_{\text{corr0}})$ against the original intensities I_{obs}, where I_{corr0} are the linearized intensities corrected by removing $R(\lambda)$ depicted by the dotted lines in Figure 6(b). As shown in panel (c) of that figure, these logarithmic ratios were fitted by a parabola. This fitted function was then removed from the corrected intensities to produce the final corrected intensities used in the Boltzmann plot of panel (a). This nonlinearity with respect to exposure was found to be negligibly small in the normal incidence region, as evidenced by Figure 6(f).

The sharp increase of sensitivity toward the short-wavelength end of Figure 6(e) may be an artifact caused by inaccuracy of the calculated A values used in our procedure or
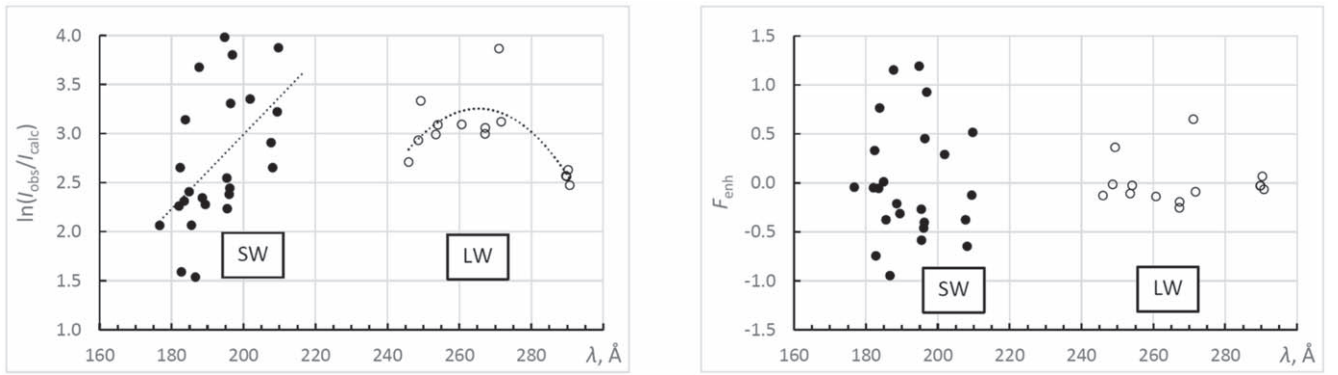
Figure 7. Reduction of the solar line intensities measured with EIS (Landi & Young 2009). Left panel: derivation of correction functions for the variation of sensitivity of the EIS instrument. The fitted linear (SW) and quadratic (LW) functions are shown by the dotted lines. Right panel: residuals of the intensity correction, which represent the enhancement factors used for intensity reduction (see the text). Blended lines are excluded from this plot. SW and LW are the short- and long-wavelength channels of the EIS instrument, respectively.

by errors in the observed intensity values given by Ekberg (1981). For a normal incidence spectrum, one would normally expect the sensitivity curve to be flat in this region. If a flat spectral response is assumed, the observed intensities of the two lines with the shortest wavelengths appear to be too large by one or two orders of magnitude. These two lines (at 1010.260 and 1263.843 Å) together with the line at 1016.072 Å correspond to the three lowest points in Figure 6(e). All three are intercombination lines with very low A values; those A values are likely to have even greater uncertainties than the rest of the lines in this figure. If these three lines are excluded from the plot, the remaining data points would be well described by a flat line. We decided not to do it because of the scarcity of observed lines in this spectral region and the poor accuracy of all calculated A values, even for LS-allowed transitions. Exclusion of three lines only on the basis of achieving the desired behavior of the spectral response curve seems too speculative, and we try to be as objective as possible. Future improvements in theory or new measurements in this region may justify a revision of the response curve. Such a revision may lead to slight changes in numerical values of reduced intensities of a few lines, but it will not affect the main results of this work. We also note that, even with the response function depicted in Figure 6(e), the shortest-wavelength line at 1010.260 Å appears to be too strong by a factor of four. Its observed wavelength deviates by 0.016 Å from the Ritz value (see Table 4). This deviation may well be explained by deformation of the photographic plate near the edge of the plate. Nevertheless, since there are at least two indications of abnormal behavior for this line, we excluded it from the least-squares fit of energy levels.

Intensities observed by Ekberg & Feldman (2003) were found to be on a roughly linear scale and are well described by a similar LTE model with $T_{eff} \approx 2.6$ eV. The response function $R(\lambda)$ of that work is practically flat in the entire region of observation, from 677 to 885 Å.

A similar LTE model also worked well for the intensities observed by Faulkner et al. (2001), despite the very different excitation mechanism in their experiment. Their effective temperature was found to be about 15 eV.

By contrast, the solar intensities reported by Landi & Young (2009) show a very strong deviation from LTE. This is not surprising, since the electron density determined from our collisional-radiative modeling (see Section 1) was very small, 8×10^8 cm^{-3}. To reduce these solar intensities to the lab scale,

we chose a different approach. Namely, we depicted the logarithms of the ratios of the observed and modeled intensities against wavelength separately in the two observation regions of EIS, 171–212 Å (SW) and 245–291 Å (LW) as shown in the left panel of Figure 7.

The fitted curves in this figure represent intensity-calibration correction functions deduced from the Fe VII intensities reported by Landi & Young (2009) and our collisional-radiative modeling. Qualitatively, these correction functions agree with findings of Del Zanna (2013) and Warren et al. (2014). Those studies demonstrated that the intensity response of both EIS channels changed in time (with an exponentially decreasing sensitivity) and as a function of wavelength. The intensity values reported by Landi & Young (2009) were determined assuming the intensity response to be the same as measured in pre-flight ground-based measurements. The trends of the correction functions determined in-flight (Del Zanna 2013; Warren et al. 2014) within a few months of the measurements of Landi & Young (2009) are similar in shape to those shown in Figure 7, although the magnitude of corrections is smaller than suggested by Figure 7. To correct the reported observed intensities, we divided them by exponents of the fitted functions represented by the dotted lines.

The right panel of Figure 7 depicts the enhancement factors F_{enh} calculated as

$$F_{enh} = \ln(I_{corr} / I_{calc}), \quad (9)$$

where I_{corr} is the corrected observed intensity, and I_{calc} is the intensity calculated by our collisional-radiative model.

Then the values of I_{corr} were reduced to our common scale by multiplying the intensities predicted for LTE conditions with our base effective temperature of 6.2 eV:

$$I_{reduced} = \frac{gA}{\lambda} \exp(-a_{base} E_{up} + F_{enh}) \quad (10)$$

(compare with Equations (4) and (8)). In this way, the experimentally observed intensities leave their footprint on the reduced values. For example, if an observed line is enhanced by an unrecognized blending, the reduced intensity will be greater than that predicted by an LTE model with the ratio given by the same enhancement factor. This is similar to what happens with the intensity reduction of laboratory data. However, in the case of our reduction of solar data, the impact of errors in the calculated atomic data on the reduced intensities

is much greater. In the reduction of the lab intensities, only the errors in *A* values influence the scale of the reduced intensities. This influence is relatively small, since errors in individual *A* values are averaged out by the fitting. With our solar intensity reduction, both the errors in our selected *A* values and the errors in collisional and radiative rates used in our modeling (from CHIANTI v.10; Del Zanna et al. 2021) affect the reduced intensities, and there is no averaging in this procedure. Thus, we expect that our final reduced intensities are less accurate (perhaps, by an additional factor of two or four, on average) for lines observed only in the EIS solar measurements.

For intensities of the forbidden lines above 2000 Å, we retained the original published values from Young et al. (2005) as observed in RR Telescopii. The *A* values of these lines are so small that they are impossible to observe in a laboratory setting, where particle densities are much larger than in the nebula, and populations of the upper levels are destroyed by collisions. Thus, it makes no sense to reduce the intensities of these lines to a scale pertinent to laboratory conditions.

We note that for lines observed in several studies, intensity values given in Table 4 are mean values of all available reduced intensities. There are 159 such averaged values. For each of them, we calculated the standard deviation from the mean. The mean of these standard deviations corresponds to a mean error by a factor of 1.8 in the individual values of reduced intensities. This gives a measure of the average accuracy of the intensity values in Table 4.

7. Ionization Energy

The ionization energy (IE) of Fe VII was previously quoted by Sugar & Corliss (1985) from Ekberg (1981) as $1,008,000(100)\,\mathrm{cm}^{-1}$. Ekberg (1981) derived it by fitting the quantum defect trends along five $3p^6 3dnf\ {}^S L_J$ series with $n = 4$ to 10 for three of them and $n = 4$–8 for the other two. As can be seen in Table 5, these series are the only ones that can be used to derive the IE, as all other available series are either too short or have an eigenvector composition that is mixed too strongly. The level values are now known more accurately than in 1981, so we have redetermined the IE. We have used a new nonlinear least-squares optimization code "fit_Ritz" developed by one of us (A.K.), which can fit several series simultaneously with a common ionization limit. This decreases the fitting error.

Only one of the five series converges to the ground level of Fe VIII, while the other four converge to the first excited level $(3p^6 3d\ {}^2 D_{5/2})$. Sugar & Corliss (1985) wrote that all Fe VIII levels are accurate to within $50\,\mathrm{cm}^{-1}$. They also wrote that the ground-term splitting of Fe VIII was determined by Cowan & Peacock (1965). The latter authors gave a value of $1840(60)\,\mathrm{cm}^{-1}$ for this splitting, while Sugar & Corliss (1985) quoted the value of $1836\,\mathrm{cm}^{-1}$ from Ramonas & Ryabtsev (1980). Unfortunately, no uncertainty was given in the latter paper. Later, Ali & Kim (1992) fitted the differences between experiment and theory for the ground-term splitting in P-like ions. Their fitted value for Fe VIII $3p^6 3d\ {}^2 D_{5/2}$ coincides with that of Ramonas & Ryabtsev (1980), and the range of residuals of their fit implies that it is accurate to about $\pm 2\,\mathrm{cm}^{-1}$. Moreover, we made a least-squares level optimization for all available observed Fe VIII lines and obtained the fine-structure splitting of $1833(3)\,\mathrm{cm}^{-1}$, also in agreement with the value of Ramonas & Ryabtsev (1980). Thus, the uncertainty of this limit offset is negligibly small compared to the quantum defect fitting uncertainty, which is $20\,\mathrm{cm}^{-1}$. The IE

value obtained in our combined fit is $1,007,928(20)\,\mathrm{cm}^{-1}$, which agrees with Ekberg's, but is five times more accurate.

8. Conclusions

The present study has extended the analysis of energy levels and spectral lines of Fe VII by combining new measurements in the vacuum ultraviolet region with all previously published experimental data. We have identified 26 new energy levels, which increased the total number of known levels to 209. The new levels were established from 72 newly identified lines observed on our spectrograms. Measurement uncertainties have been evaluated not only for our observed wavelengths, but also for those of previously published works. These data were used to optimize the energy levels. This least-squares optimization significantly reduced the uncertainties of most previously known levels. It also allowed us to compute the uncertainties of the Ritz wavelengths and redetermine the ionization limit with a fivefold improvement in accuracy. Observed intensities of all lines reported in laboratory and solar experiments have been reduced to a common linear scale. The energy level structure has been interpreted by a parametric least-squares fit of experimental energy levels using Cowan's pseudorelativistic Hartree–Fock suite of codes. This allowed us to compute radiative transition probabilities (TPs) with a reasonably high accuracy. Our newly calculated TPs have been compared with the previously published data. Uncertainties of all of these TP data sets including ours have been evaluated, and the most accurate value has been selected for each transition.

Despite a considerable improvement in accuracy of theoretical calculations in the last two decades, there are many unsolved problems in the interpretation of this Ca-like spectrum. Even the most accurate calculations cannot reproduce the order of experimental energy levels, and agreement of calculated energies with experiment is far from perfect. Most of the calculated transition probabilities are of very poor accuracy: half of our recommended best TP values are of categories D+ (uncertainty $\leqslant 40\%$) and D ($\leqslant 50\%$), and an additional 14% of them are accurate only to a factor of 2 or worse. Nevertheless, these critically evaluated data contain information that can be used to diagnose solar and other astrophysical plasmas and provide a benchmark for further development of atomic theory.

ORCID iDs

Alexander Kramida https://orcid.org/0000-0002-0788-8087
Alexander N. Ryabtsev https://orcid.org/0000-0002-5321-5406
Peter R. Young https://orcid.org/0000-0001-9034-2925

References

Ali, M. A., & Kim, Y.-K. 1992, JOSAB, 9, 185
Azarov, V. I., Kramida, A., & Vokhmentsev, M. Y. 2018, CoPhC, 225, 149
Azarov, V. I., Podobedova, L. I., & Ryabtsev, A. N. 1996, PhyS, 53, 398
Beiersdorfer, P., & Träbert, E. 2018, ApJ, 854, 114
Bowen, I. S. 1960, ApJ, 132, 1
Bowen, I. S., & Edlén, B. 1939, Natur, 143, 374
Brown, C. M., Feldman, U., Seely, J. F., Korendyke, C. M., & Hara, H. 2008, ApJS, 176, 511
Cady, W. M. 1933, PhRv, 43, 322

Cowan, R. D. 1981, The Theory of Atomic Structure and Spectra (Berkeley, CA: Univ. California Press)

Cowan, R. D., & Peacock, N. J. 1965, ApJ, 142, 390

Darnley, M. J., Henze, M., Bode, M. F., et al. 2016, ApJ, 833, 149

Del Zanna, G. 2009, A&A, 508, 501

Del Zanna, G. 2013, A&A, 555, A47

Del Zanna, G., Dere, K. P., Young, P. R., & Landi, E. 2021, ApJ, 909, 38

Dopita, M. A., Seitenzahl, I. R., Sutherland, R. S., et al. 2016, ApJ, 826, 150

Eissner, W., Jones, M., & Nussbaumer, H. 1974, CoPhC, 8, 270

Ekberg, J. O. 1975, PhyS, 11, 23

Ekberg, J. O. 1981, PhyS, 23, 7

Ekberg, J. O., & Feldman, U. 2003, ApJS, 148, 567

Ekman, J., Godefroid, M., & Hartman, H. 2014, Atoms, 2, 215

Engström, L. 1998, GFit, A Computer Program to Determine Peak Positions and Intensities in Experimental Spectra, Lund Reports in Atomic Physics LRAP-232, (Lund Univ.), https://www.atomic.physics.lu.se/fileadmin/atomfysik/AF_Personal/Professors/GFit.html

Faulkner, R., Wang, M., Dunne, P., et al. 2001, JPhB, 34, 593

Fawcett, B. C., & Cowan, R. D. 1973, SoPh, 31, 339

Feuchtgruber, H., Lutz, D., Beintema, D. A., et al. 1997, ApJ, 487, 962

Fuhr, J. R., Martin, G. A., & Wiese, W. L. 1988, JPCRD, 17, Suppl. 4

Kramida, A. 2006, NIST Atomic Energy Levels and Spectra Bibliographic Database, v2.0 (Gaithersburg, MD: National Institute of Standards and Technology)

Kramida, A. 2013, Fus. Sci. Technol., 63, 313

Kramida, A. 2014a, ApJS, 212, 11

Kramida, A. 2014b, Atoms, 2, 86

Kramida, A. 2019, A Suite of Atomic Structure Codes Originally Developed by R. D. Cowan Adapted for Windows-based Personal Computers (NIST Public Data Repository)

Kramida, A. E. 2011, CoPhC, 182, 419

Kramida, A., Ralchenko, Y., Reader, J. & NIST ASD Team. 2020, NIST Atomic Spectra Database, v5.8 (Gaithersburg, MD: National Institute of Standards and Technology), https://physics.nist.gov/asd

Kurucz, R. L. 2010, Calculated Atomic Data for Fe VII, http://kurucz.harvard.edu/atoms/2606/

Landi, E., & Young, P. R. 2009, ApJ, 706, 1

Li, Y., Xu, X., Li, B., Jönsson, P., & Chen, X. 2018, MNRAS, 479, 1260

Liang, G. Y., Baumann, T. M., López-Urrutia, J. R. C., et al. 2009, ApJ, 696, 2275

Malinovsky, L., & Heroux, M. 1973, ApJ, 181, 1009

McKenna, F. C., Keenan, F. P., Hambly, N. C., et al. 1997, ApJS, 109, 225

Moore, C. E. 1952, Atomic Energy Levels, National Bureau of Standards (U.S.) Circular 467, Vol. 2 (Washington, DC: US Government Printing Office)

Nielson, C. W., & Koster, G. F. 1963, Spectroscopic Coefficients for the p^n, d^n, and f^n Configurations (Cambridge, MA: MIT Press)

Nussbaumer, H., & Storey, P. J. 1982, A&A, 113, 21

Peck, E. R., & Reeder, K. 1972, JOSA, 62, 958

Perinotto, M., Bencini, C. G., Pasquali, A., et al. 1999, A&A, 347, 967

Radziemski, L. J., Jr., & Kaufman, V. 1969, JOSA, 59, 424

Ramonas, A. A., & Ryabtsev, A. N. 1980, OptSp, 48, 348

Reader, J., & Sugar, J. 1975, JPCRD, 4, 353

Rose, M., Tadhunter, C. N., Holt, J., Ramos Almeida, C., & Littlefair, S. P. 2011, MNRAS, 414, 3360

Ryabtsev, A. N. 2017, EPJWC, 132, 03043

Sugar, J., & Corliss, C. 1985, Atomic Energy Levels of the Iron-period Elements: Potassium through Nickel (Washington, DC: American Chemical Society)

Svensson, L. A., & Ekberg, J. O. 1969, Akr. Fys., 40, 145

Tayal, S. S., & Zatsarinny, O. 2014, ApJ, 788, 24

Warner, B., & Kirkpatrick, R. C. 1969a, Oscillator Strengths in the Sc II Isoelectronic Sequence (Austin, TX: Department of Astronomy, Univ. Texas)

Warner, B., & Kirkpatrick, R. C. 1969b, MNRAS, 144, 397

Warren, H. P., Ugarte-Urra, I., & Landi, E. 2014, ApJS, 213, 11

Witthoeft, M. C., & Badnell, N. R. 2008, A&A, 481, 543

Wyatt, M., & Nave, G. 2017, ApOpt, 56, 3744

Young, P. R., Berrington, K. A., & Lobel, A. 2005, A&A, 432, 665

Young, P. R., Feldman, U., & Lobel, A. 2011, ApJS, 196, 23

Young, P. R., & Landi, E. 2009, ApJ, 707, 173

Young, P. R., Ryabtsev, A. N., & Landi, E. 2021, ApJ, 908, 104

Zeng, J., Liang, G. Y., Zhao, G., & Shi, J. R. 2005, MNRAS, 357, 440